minerals

MDPI

Article

Nataliakulikite, $Ca_4Ti_2(Fe^{3+},Fe^{2+})(Si,Fe^{3+},Al)O_{11}$, a New Perovskite-Supergroup Mineral from Hatrurim Basin, Negev Desert, Israel

Victor V. Sharygin [1,2,3,*], Grigory A. Yakovlev [3], Richard Wirth [4], Yurii V. Seryotkin [1,2], Ellina V. Sokol [1], Elena N. Nigmatulina [1], Nikolai S. Karmanov [1] and Leonid A. Pautov [5,6]

1 V.S. Sobolev Institute of Geology and Mineralogy, Siberian Branch of the RAS, 3 Acad. Koptyuga pr., Novosibirsk 630090, Russia; yuvs@igm.nsc.ru (Y.V.S.); sokol_ag@mail.ru (E.V.S.); helena@igm.nsc.ru (E.N.N.); krm@igm.nsc.ru (N.S.K.)
2 Department of Geology and Geophysics, Novosibirsk State University, 2 Pirogov str., Novosibirsk 630090, Russia
3 ExtraTerra Consortium, Institute of Physics and Technology, Ural Federal University, 19 Mira str., Ekaterinburg 620002, Russia; yakovlev.grigoriy@gmail.com
4 Helmholtz Centre Potsdam, GFZ German Research Centre for Geosciences, Section 3.3, Telegrafenberg, 14473 Potsdam, Germany; richard.wirth@gfz-potsdam.de
5 A.E. Fersman Mineralogical Museum RAS, 18/2 Leninskiy pr., 115162 Moscow, Russia; pla58@mail.ru
6 Institute of Mineralogy, Uralian Branch of the RAS, Miass 456317, Russia
* Correspondence: sharygin@igm.nsc.ru; Tel.: +7-383-330-80-84

Received: 18 October 2019; Accepted: 8 November 2019; Published: 13 November 2019

Abstract: Nataliakulikite, $Ca_4Ti_2(Fe^{3+},Fe^{2+})(Si,Fe^{3+},Al)O_{11}$, is a mineral intermediate between perovskite $CaTiO_3$ and brownmillerite $Ca_2(Fe,Al)_2O_5$. It was discovered as a minor mineral in a high-temperature pyrometamorphic larnite-gehlenite rock at the Nahal Morag Canyon of the Hatrurim Basin, Israel. Nataliakulikite is associated with larnite, flamite, gehlenite, magnesioferrite, Fe^{3+}-rich perovskite, fluorapatite, barite, Hashemite, and retrograde phases (afwillite, hillebrandite, portlandite, calcite, ettringite, hydrogarnet, and other hydrated Ca-silicates). The mineral forms brown subhedral or prismatic grains (up to 20 μm) and their intergrowths (up to 50 μm). Its empirical formula (n = 47) is $(Ca_{3.992}Sr_{0.014}U_{0.004})(Ti_{1.933}Zr_{0.030}Nb_{0.002})$ $(Fe^{3+}{}_{0.610}Fe^{2+}{}_{0.405}Cr_{0.005}Mn_{0.005})(Si_{0.447}Fe^{3+}{}_{0.337}Al_{0.216})O_{11}$ and shows Si predominance in tetrahedral site. The unit-cell parameters (HRTEM data) and space group are: a = 5.254, b = 30.302, c = 5.488 Å, V = 873.7 Å^3, *Pnma*, Z = 4. These dimensions and Electron backscatter diffraction (EBSD) data strongly support the structural identity between nataliakulikite and synthetic $Ca_4Ti_2Fe^{3+}{}_2O_{11}$ ($2CaTiO_3{\cdot}Ca_2Fe^{3+}{}_2O_5$), an intermediate compound in the system $CaTiO_3$-$Ca_2Fe^{3+}{}_2O_5$. In general, this mineral is a Si-Fe^{2+}-rich natural analog of synthetic $Ca_4Ti_2Fe^{3+}{}_2O_{11}$. The X-ray powder diffraction data (Cu$K\alpha$ -radiation), calculated from unit-cell dimensions, show the strongest lines {d [Å], (I_{calc})} at: 2.681(100), 1.898(30), 2.627(26), 2.744(23), 1.894(22), 15.151(19), 1.572(14), 3.795(8). The calculated density is 4.006 g/cm^3. The crystal structure of nataliakulikite has not been refined because of small sizes of grains. The Raman spectrum shows strong bands at 128, 223, 274, 562, and 790 cm^{-1}. Nataliakulikite from the Hatrurim Basin crystallized under the conditions of combustion metamorphism at high temperatures (1160–1200 °C) and low pressures (HT-region of the spurrite-merwinite facies).

Keywords: nataliakulikite; perovskite-brownmillerite series; perovskite supergroup; larnite-gehlenite rock; pyrometamorphism; combustion metamorphism; Hatrurim Basin; Israel

1. Introduction

The natural Si-Fe^{2+}-rich analog of the orthorhombic synthetic phase $Ca_4Ti_2Fe^{3+}{}_2O_{11}$, an intermediate member between perovskite $CaTiO_3$ and brownmillerite Ca_2FeAlO_5, named nataliakulikite, was discovered in a larnite-gehlenite rock at the Hatrurim Basin, the largest combustion metamorphism complex of the Hatrurim Formation on the territory of Israel [1–5].

Synthetic Fe-rich compounds based on the perovskite and brownmillerite structures ("layered perovskites") have been intensively studied in material sciences due to their superconductivity and ion-conductivity properties [6,7]. The phase, $Ca_4Ti_2Fe^{3+}{}_2O_{11}$, was firstly synthesized in the 1980s [8]. At present, three synthetic ordered phases, intermediate between brownmillerite Ca_2FeAlO_5 and perovskite $CaTiO_3$, are known: $Ca_4Ti_2Fe^{3+}{}_2O_{11}$ [8,9], $Ca_3TiFe^{3+}{}_2O_8$ [10–12], and $Ca_5TiFe^{3+}{}_2Al_2O_{13}$ [13].

Nataliakulikite $Ca_4Ti_2(Fe^{3+},Fe^{2+})(Si,Fe^{3+},Al)O_{11}$ was approved by the Commission on New Minerals, Nomenclature and Classification (CNMNC) of the International Mineralogical Association (IMA) as a new mineral species in September 2018 (IMA 2018-061). The mineral is named in honor of Natalia Artyemovna Kulik (b. 1933) from Novosibirsk, Russia, a well-known Russian mineralogist, a reputed expert in mineralogical descriptions of granitic pegmatites [14], minerals of radioactive and rare-earth elements and archaeometry [15–17]. She is Emeritus Professor of Mineralogy at the Novosibirsk State University, who during the last 40 years has been teaching hundreds geologists and mineralogists, including some of the authors of this paper. Nataliakulikite is an essential mineral in high-temperature larnite-gehlenite rock found in the Nahal Morag Canyon of the Hatrurim Basin, Israel (Figure 1). The holotype sample of a larnite-gehlenite rock containing abundant nataliakulikite (author number W11-3, see [18,19]) is deposited in the Central Siberian Geological Museum of the V.S. Sobolev Institute of Geology and Mineralogy, Novosibirsk (number VII-101/1). Previously this mineral was described in the Hatrurim larnite rocks as a Si-Fe^{2+}-rich natural analog of synthetic $Ca_4Ti_2Fe^{3+}{}_2O_{11}$ [18]. In general, nataliakulikite is a last natural analog for the important key phases on the phase diagram $CaTiO_3$-$CaFe_2O_5$ [20–22]. According to the recent nomenclature of the perovskite supergroup [23], it belongs to the anion deficient perovskites (brownmillerite subgroup, non-stoichiometric perovskites group). Brownmillerite $Ca_2Fe^{3+}AlO_5$, srebrodolskite $Ca_2Fe^{3+}{}_2O_5$, shulamitite $Ca_3TiFe^{3+}AlO_8$ and sharyginite $Ca_3TiFe^{3+}{}_2O_8$ are other members of this subgroup [24–31].

The occurrences of the Hatrurim Formation (and Hatrurim Basin in first order) are becoming a "mineralogical Mecca" due to numerous findings of new minerals in unique pyrometamorphic rocks [1,32]. Hatrurim Basin is type locality for bayerite, bentorite, ye'elimite, grossite, hatrurite, and nagelschmidtite [1,33–36]. In last decade more than 20 new minerals were found within the Hatrurim Basin: barioferrite, shulamitite, murashkoite, zadovite, gurimite, hexacelsian, aradite, gazeevite, stracherite, ariegilatite, fluorkyuygenite, negevite, halamishite, zuktamrurite, transjordanite, silicocarnotite, khesinite, flamite, polekhovskyite, zoharite, gmalimite, nazarovite, and others [30,37–57]. Most of them were identified in larnite and spurrite rocks and Ca-rich paralavas; and some of them may be used as indicator minerals to estimate the history of rock formation. For example, the shulamitite/sharyginite association with Fe^{3+}-perovskite from the Hatrurim Basin larnite rocks records crystallization under high temperatures (1150–1170 °C) and low pressures (high-T-region of the spurrite-merwinite facies). Coexistence of flamite and larnite in the Hatrurim Ca-Al-rich paralavas reveals specific cooling history (quenching of melt) during their solidification [52].

In this paper, we provide a detailed description of nataliakulikite. Some data on nataliakulikite-bearing rocks from the Hatrurim Basin were reported in a few previous publications [5,18,19].

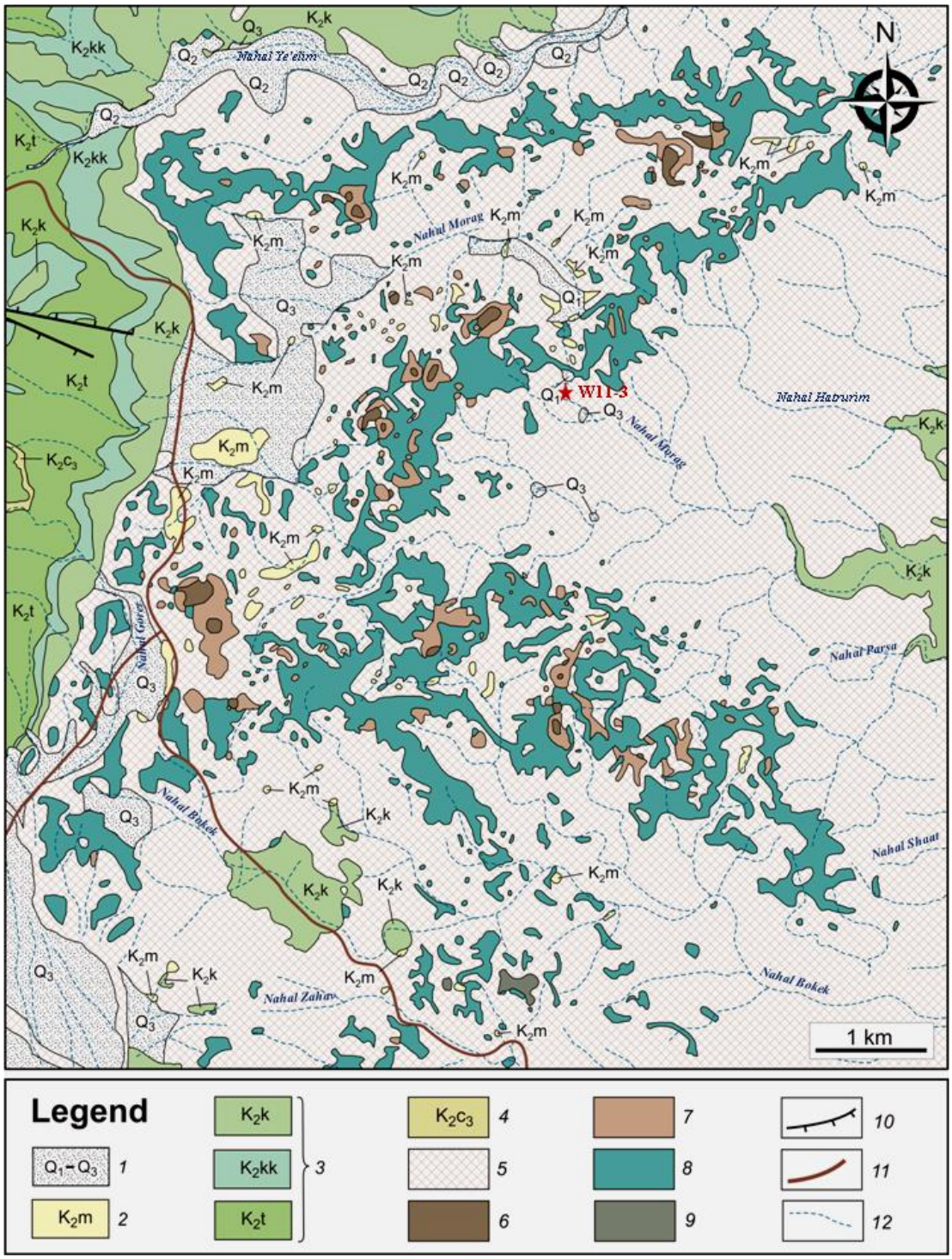

Figure 1. Schematic geological map of the northwestern Hatrurim Basin, modified after the 1:50,000 Geological Map of Israel [58]. 1—Pleistocene terrace conglomerates (Q_1, Q_2, Q_3); 2—Maastrichtian organic-rich marine chalk (K_2m); 3—Campanian (K_2k), Santonian (K_2kk), and Turonian (K_2t) limestone, chalk, and dolomite with chert and phosphorite intercalations; 4—Cenomanian (K_2c_3) limestone, dolomite, and chalk; 5—Low-grade Hatrurim Fm rocks; 6—Larnite rocks (High-grade Hatrurim Fm rocks); 7—"Olive rocks" (Hatrurim Fm); 8—Spurrite marbles (medium-grade Hatrurim Fm rocks); 9—Pseudo-conglomerates; 10—Faults; 11—Road; 12—Wadi. Red star marks the sampling site of W11-3 rock with nataliakulikite in the Nahal Morag Canyon.

2. Brief Geological Background for Haturim Basin

The Hatrurim Basin is one of the largest complexes in the Hatrurim Formation (also known as "Mottled Zone", MZ) in the territories of Israel and Jordan. All Hatrurim Fm. occurrences are localized along the Jordanian-Dead Sea transform fault and are composed of brecciated chalky and marly sediments and metamorphic rocks of the spurrite-merwinite facies, locally altered under low-temperature hydrous conditions [1,4,5].

The specific non-stratigraphic unit of the MZ rocks lies at the top of the Upper Cretaceous–Low Tertiary section and reaches depths from 30 to 120 m below the surface [1]. The term *MZ sequence* refers to highly diverse sedimentary rocks which underwent post-depositional alteration under highly contrasting conditions. The Hatrurim Basin territory abounds in conical hills composed of spurrite marbles, medium-temperature (T ~ 700–800 °C) combustion metamorphic (CM) rocks, in their lower and middle parts. The rocks, as well as their hydrated varieties, up to 4 m thick, commonly cover large areas (Figure 1). Their upper part consists of coarse-clastic breccias with lumps of marl, limestone, phosphorite, and flint from the strata below. Local spots of the so-called "olive unit" [1,2,59] are restricted to the hill top parts. The highly porous rocks of the olive unit are mainly composed of calcite and zeolite, which cement quartz sand particles and clasts of the underlying sediments. Other rocks of the unit are high-temperature clinopyroxene-anorthite hornfels and paralavas which form specific swells and "ploughed land" structures [59,60].

High-temperature larnite-bearing rocks (T = 1000–1400 °C) were found at several levels of the Hatrurim Fm. section, mainly in the northern and central parts of the Hatrurim Basin (Figure 1). In the lower section within 20 m above the basement, they are from a few tens of centimeters to a few meters thick and neighbour gehlenite hornfels bodies. Both larnite and gehlenite CM rocks can easily transform into pseudoconglomerates with remnant "pebbles" or "cobbles" (from 1–2 to 15–20 cm in diameter) by retrograde hydration and/or carbonation. The secondary products are mainly calcite, aragonite, gypsum, ettringite, and minor Ca silicate-hydrates. Larnite rocks occur as isolated mottles (to 10 m across) among strongly altered varieties. At hilltops, monolithic larnite rocks make up separate isometric massive blocks, plates or cliff scarps, up to 50 m across and 10 m thick [1,2,5,26,30]. Descriptions of individual bodies of these rocks is given in [1–5,26,30,59–64].

Many authors interpreted the Hatrurim Fm. complexes as products of in situ combustion of low-calorific fuel, specifically disseminated bituminous matter of marine chalk [2,3,65–68]. Other authors attributed CM events within the Hatrurim Fm. complexes to local breakthrough and ignition of high-calorific hydrocarbon gases, mainly methane, which may result from mud volcanism [4,5,26,30,52,59,60,63,64,69,70]. Emissions of hydrocarbon gases in the geological past left imprint in abundant foci of high- (800–1100 °C) and ultrahigh-temperature (1200–1500 °C) combustion metamorphism of sediments in the Hatrurim Basin and other MZ localities [26,30,59,60,63,64]. Burning of high-calorific fossil fuel released enough heat to maintain CM alteration and local melting of marly sediments. The burnt carbonate rocks transformed into diverse calcium-rich metamorphic rocks with typical clinker mineralogy [26], whereas marly sediments melted at the same temperature and formed clinopyroxene-bearing paralavas [59].

Despite the controversy about their genesis, all metamorphic rocks of the Hatrurim Basin and other MZ localities are considered to be products of high-temperature (700–1200 °C) solid-state reactions during organic matter combustion, sometimes with further local melting events at 1250–1500 °C [5,26,30,32,41,44,52,59–65,70–73].

3. Analytical Methods

Double-polished rock sections (~50 μm in thickness) were used for transmitted and reflected light microscope examination of the Hatrurim larnite-gehlenite rock with nataliakulikite (Figure 3). During the preparation of polished samples, no water-bearing abrasives were used. Identification of minerals was based on energy-dispersive spectra (EDS), back-scattered electron (BSE) images and elemental mapping (EDS system), using a TESCAN MIRA 3MLU scanning electron microscope equipped with

an INCA Energy 450 XMax 80 microanalysis system (Oxford Instruments Ltd., Abingdon, UK) at the V.S. Sobolev Institute of Geology and Mineralogy (IGM), Novosibirsk, Russia. EDS analyses of minerals were done in high-vacuum modes at an accelerating voltage of 20 kV, a probe current of 1 nA, and accumulation time of 20 s. The following synthetic compounds, minerals, and pure metals were used as reference standards for most of the elements: SiO_2 (Si and O), Al_2O_3 (Al), diopside (Mg and Ca), albite (Na), orthoclase (K), $Ca_2P_2O_7$ (P), BaF_2 (Ba and F), Cr_2O_3 (Cr), $CsRe_2Cl_6$ (Cl), $LaPO_4$ (La), $CePO_4$ (Ce), SrF_2 (Sr), metallic Ti, Fe, Mn, Zn, Ni, V and Cu. Correction for matrix effects was done using the XPP algorithm, implemented in the software of the microanalysis system. Metallic Co served for quantitative optimization (normalization to probe current and energy calibration of the spectrometer).

Electron microprobe analyses (EMPA) in wavelength-dispersive (WDS) mode were performed for nataliakulikite and related minerals from the Hatrurim larnite-gehlenite rocks using a JXA-8100 microprobe (Jeol Ltd., Tokyo, Japan) at IGM. Grains (sizes > 5 μm), which were previously analyzed by EDS, were selected for this purpose. The operating conditions were as follows: Beam diameter of 1–2 μm, accelerating voltage of 20 kV, beam current of 30 nA, and counting time of 10 (5 + 5) s. The following standards were used for nataliakulikite and related opaque minerals: Natural wollastonite (Ca and Si) and ilmenite (Ti), synthetic $MgAl_2O_4$ (Al and Mg), MnO (Mn), Fe_2O_3 (Fe), $NiFe_2O_4$ (Ni), $ZnFe_2O_4$ (Zn), Cr_2O_3 (Cr), zircon (Zr), $LiNbO_3$ (Nb), UO_2 (U), Sr-silicate glass (Sr), and Cu_2O (Cu). Correction for matrix effects was done using a PAP routine [74]. The precision of analysis for major elements was better than 2% relative. The detection limits for elements are (in ppm): Si—207; Ti—116; Cr—128; Al—170; Fe—107; Mn—140; Mg—147; Ca—159; Cu—132; U—251; Sr—163; Ni—132; Zn—266; Zr—254; Nb—227.

The Raman spectra were recorded on a LabRAM HR 800 mm (HORIBA Scientific Ltd., Lat Krabang, Thailand) spectrometer equipped with a 1024 pixel LN/CCD detector and coupled to an Olympus BX40 confocal microscope (Objective X100, Tokyo, Japan) at IGM. A semiconductor laser emitting at 514.5 nm with a nominal power output of 50 mW was used for excitation. In each case, 20 spectra were recorded for 20 s each at a hole diameter of 100 μm and integrated. The spectra were recorded between 100 and 1200 cm^{-1}, and the monochromator was calibrated using the 520.7 cm^{-1} Raman line of elemental Si.

High-resolution transmission electron microscopy (HRTEM) study for FIB-milled foils with nataliakulikite was performed with a TECNAI F20 X-Twin transmission electron microscope (FEI Company, Hillsboro, OR, USA) with a field emission gun FEG as electron source at Helmholtz Centre Potsdam, GFZ, Germany [75,76]. The point resolution is 0.25 nm and the lattice resolution is 0.102 nm with an information limit of 0.14 nm. The TEM is equipped with a GATAN Tridiem imaging filter GIF™ and all HRTEM images were acquired as energy-filtered images applying a 10 eV window to the zero-loss peak. A careful correction of astigmatism of the objective lens was performed using the Digital Micrograph software package. Electron diffraction patterns were recorded on image plates and calculated from high-resolution images using Fast Fourier Transform (FFT) software packages. Phase identification was made by measuring the lengths of the different vectors in the diffraction patterns and calculating the respective d_{hkl}-spacing. Additionally, the angles between adjacent vectors were measured in the diffraction patterns. The d_{hkl}-spacing is precise to within three decimals of a nanometer. The angles between the vectors were determined with an accuracy of 0.5°.

Quantitative reflectance measurements for nataliakulikite from the Hatrurim Basin were provided in air relative to a SiC standard using a UMSP 50D Opton microscope-spectrophotometer (Carl Zeiss, Jena, Germany) at the A.E. Fersman Mineralogical Museum RAS, Moscow, Russia.

Electron backscatter diffraction studies were provided for two grains of nataliakulikite. Thin sections intended for EBSD studies were subjected to polishing by Buehler MasterMet2 non-crystallizing colloidal silica suspension (0.02 μm). EBSD measurements were carried out by means of a FE-SEM ZEISS SIGMA VP scanning electron microscope equipped with an Oxford Instruments Nordlys HKL EBSD detector, operated at 20 kV and 1.4 nA in focused beam mode with a 70° tilted stage at Institute of Physics and Technology, Ural Federal University, Ekaterinburg, Russia. Structural identification of

nataliakulikite was performed by matching its EBSD patterns with the reference structural models using program FLAMENCO.

4. Sample Description

Nataliakulikite was discovered in the rocks at the Nahal Morag Canyon, in the central part of the Hatrurim Basin, the Negev desert (approximately 5 km to southeast from Arad, Israel). Latitude—31°13′20.41″ N, longitude—35°17′43.81″ E (Figure 1). In general, it is located near "fair foci" described by Burg et al. [2].

This mineral was found in a larnite-gehlenite fine-grained rock occurring as a brown-gray pebble in "pseudoconglomerates" in the southern part of the Nahal Morag Canyon at Hatrurim Basin (Figures 2 and 3). The pebble is characterized by specific microbending due to alternation of microlayers enriched in red-colored oxides and silicates (Figure 3).

The high-temperature mineral assemblage of the holotype rock sample (W11-3) includes larnite, flamite, gehlenite, magnesioferrite, nataliakulikite, Fe^{3+}-rich perovskite, fluorapatite, barite, and hashemite [18]. In addition unidentified K-Ca-Ba-chromate (up to 5 μm) has been found (EDS, n = 4; K_2O—12.6, BaO—28.7, SrO—0.4, CaO—9.1, FeO—2.0, Cr_2O_3—26.3, SiO_2—5.9, SO_3—3.5 wt.%, possible solid solution between tarapacáite K_2CrO_4 and hashemite $BaCrO_4$). Retrograde phases are afwillite, hillebrandite, portlandite, calcite, ettringite, hydrogarnet, and hydrated P-S-rich Ca-silicates after larnite and flamite. Altered areas of the rock (Figure 3) have a white color and are mainly confined to the outer parts of the "pebble". In general, the first signs of retrograde transformation (whitening of rock) are related to the replacement of larnite and flamite by hydrated P-S-rich Ca-silicates.

Magnesioferrite is a main opaque mineral in the rock. Nataliakulikite is minor with respect to magnesioferrite, but it is a predominant member of the perovskite-brownmillerite series in the holotype sample, with its bulk content of ~5 vol.% (Figures 4 and 5). Major and trace element composition of the W11-3 holotype sample were previously reported [5]. The data on the chemistry of the main rock-forming minerals are summarized in Table 1.

Figure 2. "Pseudoconglomerates" with pebbles of nataliakulikite-bearing rocks, Nahal Morag Canyon, Hatrurim Basin, Israel, photographs taken in February 2019.

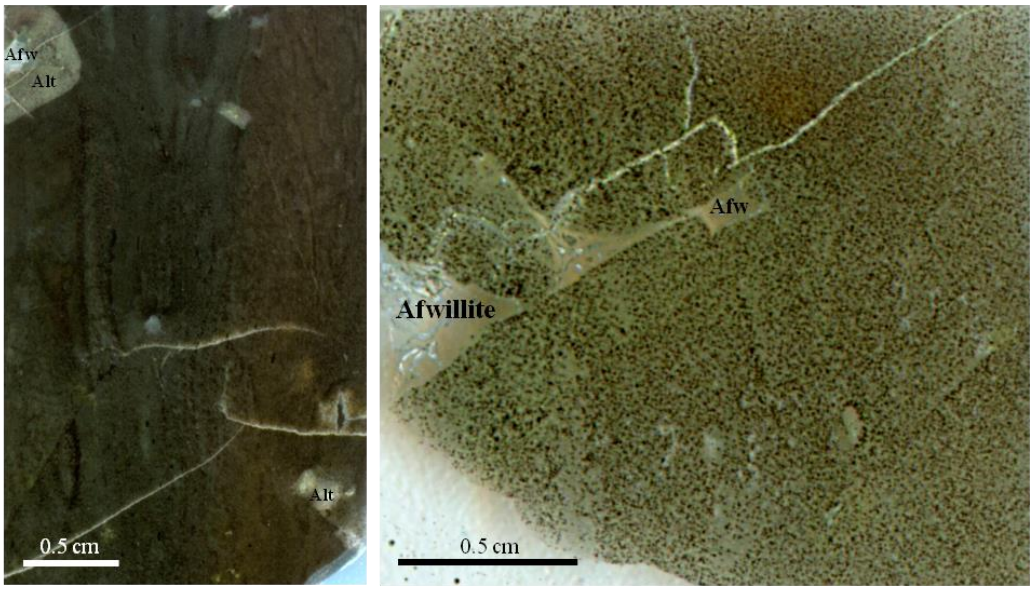

Figure 3. General view of fine-grained larnite-gehlenite rock with nataliakulikite (holotype sample W11-3), Nahal Morag Canyon, Hatrurim Basin, Israel (ordinary and transmitted light). Afw—afwillite; Alt—whitened and altered areas of the rock.

Note that among main minerals, only gehlenite shows essential core-to-rim variations with increasing of the *ferrigehlenite* end-member. Individual grains of fluorapatite are variable in the P_2O_5, SiO_2 and SO_3 contents. Magnesioferrite is rich in CuO (0.4), ZnO (0.7), NiO (0.8), and CaO (up to 1.5 wt.%). Larnite and flamite form regular lamellar intergrowths like in Ca-Al-rich paralavas at Hatrurim Basin [52], but rarely occur as individual grains. Both minerals differ in the contents of CaO, SiO_2, P_2O_5, and total alkalis (Table 1). Perovskite, barite, and hashemite occur very rarely. In general, the petrography of the studied sample indicates that this rock seems to be formed due to high-temperature solid-phase reactions without melting.

In general, individual pebbles and even different parts of concrete pebbles in the Nahal Morag Canyon "pseudoconglomerate" section may have contrasting colors and mineral compositions (Figure 2). For example, larnite-gehlenite pebbles, which are nataliakulikite-bearing rock neighbours, do lack nataliakulikite and may include either rankinite, Ti-andradite-schorlomite, khesinite, trevorite, hematite, perovskite and kalsilite (yellowish W11-2-1) or magnesioferrite, sharyginite, perovskite and khesinite (brownish W11-2-2).

5. Morphology, Optical and Physical Properties of Nataliakulikite

Nataliakulikite commonly occurs in the holotype sample as a subhedral or prismatic grains (up to 20 μm) and their intergrowths (up to 50 μm). Usually, the size of nataliakulikite grains is less than 10 μm (Figures 4–6); it is smaller than that of neighboring magnesioferrite and silicates. The color of this mineral is brown and it is easily distinguishable optically from the dark red magnesioferrite in transmitted and reflected light and on BSE images. The color of the powdered mineral is light brown. Nataliakulikite has submetallic to opaque luster. Its hardness is ≈5.5–6 (Mohs), microhardness VHN_{20} = 531 kg/mm^2 (n = 1). Cleavage and parting are none observed, fracture is uneven. Density was not measured directly because of small grain size and common inclusions. Density (4.006 g/cm^{-3}) was calculated from unit-cell dimensions and results of electron-microprobe analyses. Under reflected light nataliakulikite is gray to light gray and shows yellowish brown internal reflections. Bireflectance and anisotropy are weak, pleochroism is distinct from gray to light gray.

The reflectance data for the mineral are given in Table 2. Reflectance percentages for the four R_{max} and R_{min} COM (Commission on Ore Mineralogy) wavelengths are: 14.15, 14.08 (470 nm); 13.45, 13.43 (546 nm); 13.20, 13.15 (589 nm), and 12.98, 12.83 (650 nm).

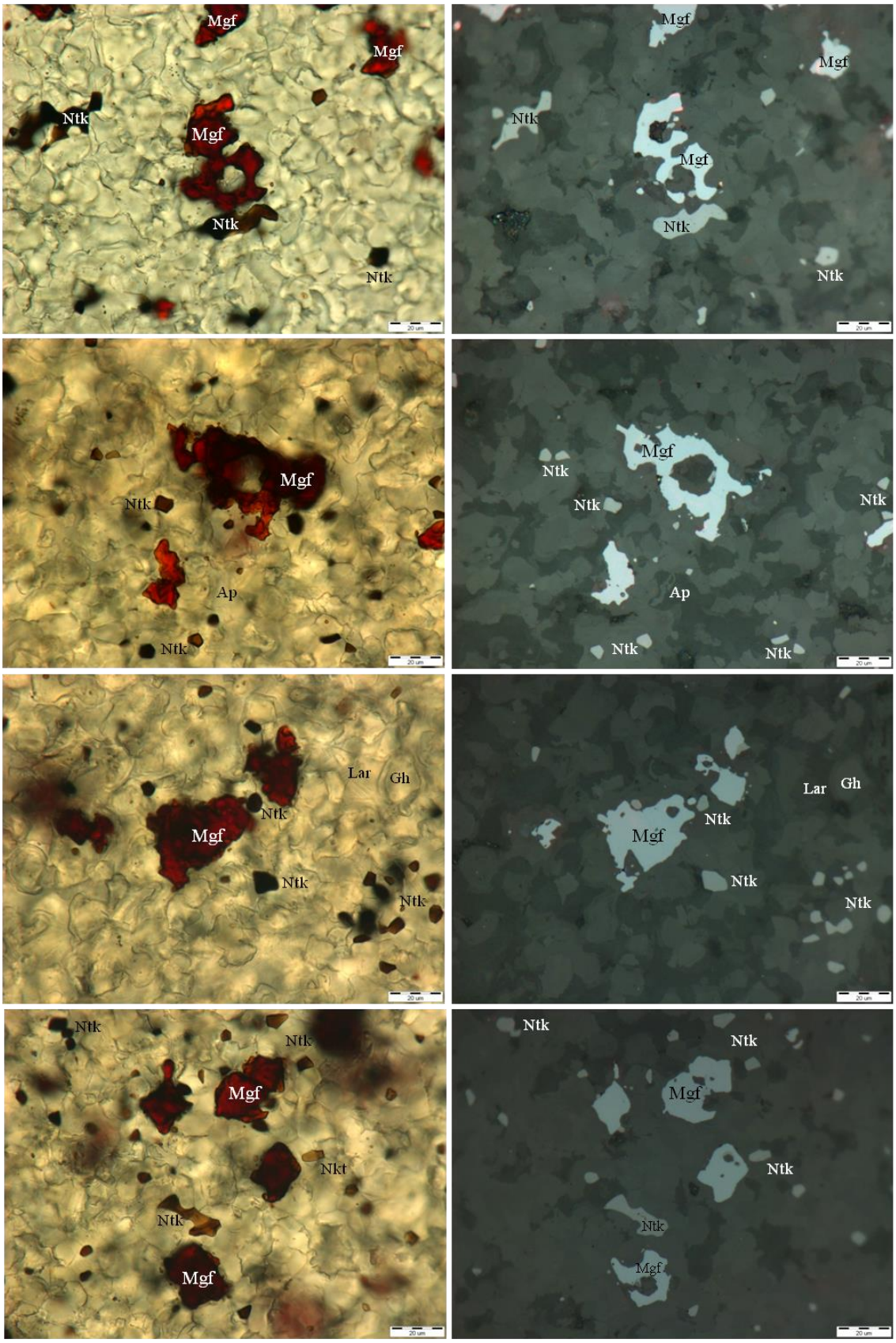

Figure 4. Nataliakulikite in larnite-gehlenite rock (holotype sample, W11-3) from Nahal Morag Canyon, Hatrurim Basin, Israel (transmitted and reflected light). Ntk—nataliakulikite; Mgf—magnesioferrite; Lar—larnite ± flamite; Gh—gehlenite; Ap—fluorapatite.

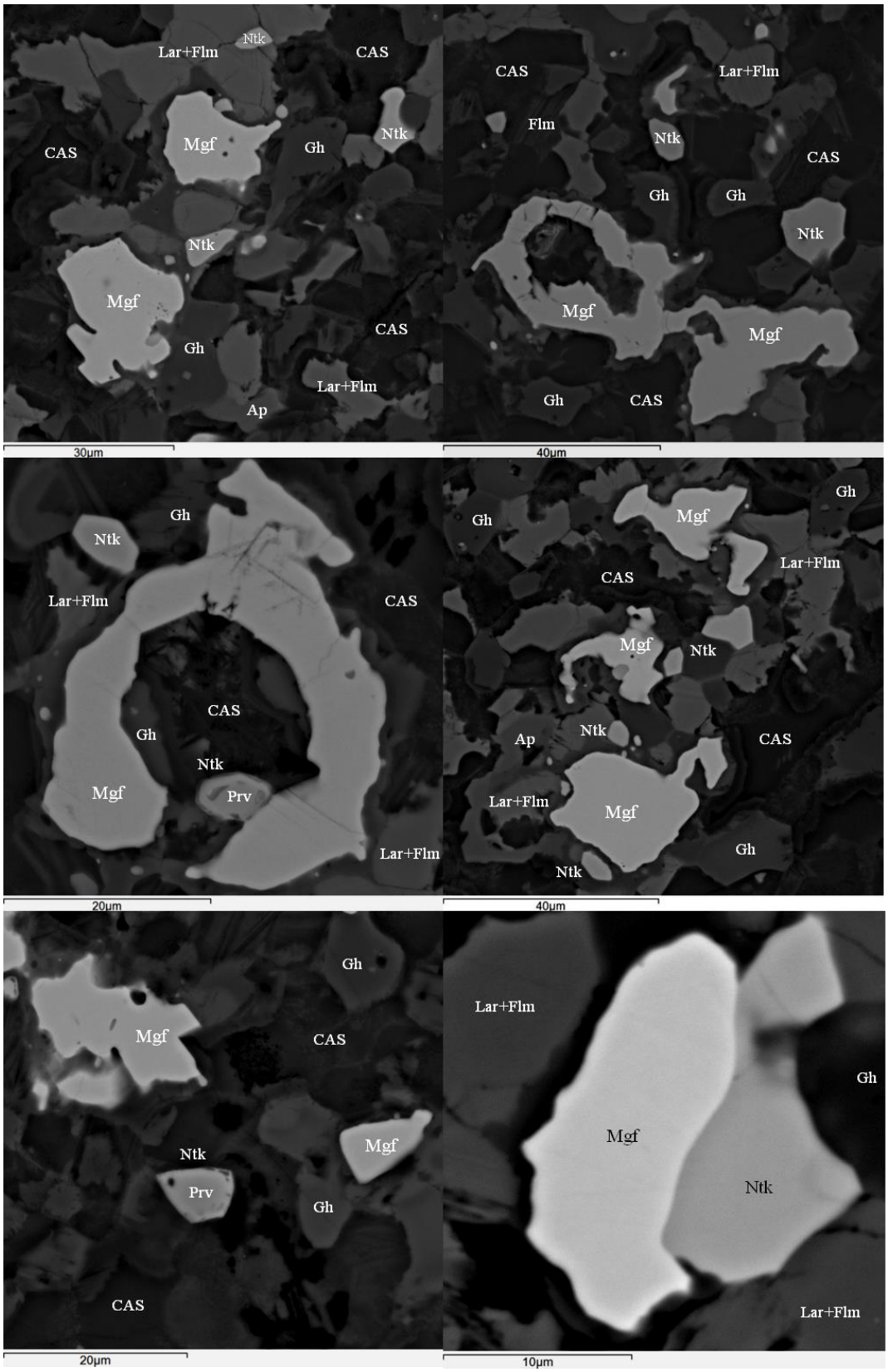

Figure 5. Back-scattered electron (BSE) images of nataliakulikite in larnite-gehlenite rock (holotype sample, W11-3) from Nahal Morag Canyon, Hatrurim Basin, Israel. Ntk—nataliakulikite; Prv—Fe-rich perovskite; Mgf—magnesioferrite; Lar—larnite; Flm—flamite; Gh—gehlenite; Ap—fluorapatite; CAS—hydrated Ca-silicates.

Table 1. Chemical composition (WDS-EDS, wt.%) of principal minerals in gehlenite-larnite rock with nataliakulikite (sample W11-3), Nahal Morag Canyon, Hatrurim Basin, Israel.

Mineral	**Gehlenite**		**Larnite**	**Flamite**	**Fluorapatite**		**Magnesioferrite**	**Perovskite**	**Barite**	**Hashemite**
Position	**core**	**rim**								
n	**36**	**7**	**26**	**18**	**3**	**2**	**45**	**6**	**7**	**6**
SiO_2	22.17	21.60	33.03	29.14	3.29	6.28	n.a.	3.81	n.a.	n.a.
TiO_2	0.04	0.00	n.d.	n.d.	n.a.	n.a.	0.01	33.36	n.a.	n.a.
ZrO_2	n.a.	n.a.	n.a.	n.a.	n.a.	n.a.	n.a.	0.74	n.a.	n.a.
Nb_2O_5	n.a.	n.a.	n.a.	n.a.	n.a.	n.a.	n.a.	0.06	n.a.	n.a.
V_2O_5	n.a.	n.a.	n.a.	n.a.	0.52	0.50	n.a.	n.a.	n.a.	n.a.
Cr_2O_3	n.a.	n.a.	n.a.	n.a.	n.a.	n.a.	0.41	0.07		
Al_2O_3	32.91	28.05	0.11	0.14	n.a.	n.a.	3.55	1.92	n.a.	n.a.
Fe_2O_3	4.25	10.48					74.01	17.66		
FeO	0.28	0.18	0.10	0.24	0.19	0.33	1.30		n.d.	n.d.
NiO	n.a.	n.a.	n.a.	n.a.	n.a.	n.a.	0.81	n.a.	n.a.	n.a.
ZnO	n.a.	n.a.	n.a.	n.a.	n.a.	n.a.	0.66	n.a.	n.a.	n.a.
CuO	n.a.	n.a.	n.a.	n.a.	n.a.	n.a.	0.44	n.a.	n.a.	n.a.
MnO	n.d.	n.d.	n.a.	n.a.	n.a.	n.a.	0.27	0.03	n.a.	n.a.
MgO	0.28	0.35	n.d.	n.d.	n.a.	n.a.	17.25	n.d.	n.a.	n.a.
CaO	40.26	39.17	63.22	59.54	55.23	55.91	1.50	41.98	0.67	0.53
BaO	n.a.	n.a.	n.a.	n.a.	n.a.	n.a.	n.a.	n.a.	62.76	61.45
SrO	n.d.	n.d.	0.27	0.37	0.83	n.a.	n.a.	0.27	0.75	0.44
Na_2O	n.d.	n.d.	0.65	0.94	n.a.	n.a.	n.a.	n.a.	n.a.	n.a.
K_2O	n.d.	n.d.	0.65	2.49	n.a.	n.a.	n.a.	n.a.	n.a.	n.a.
P_2O_5	n.d.	n.d.	2.26	6.98	37.53	29.31	n.a.	n.a.	n.a.	n.a.
SO_3	n.a.	n.a.	n.d.	n.d.	0.82	6.27	n.a.	n.a.	18.91	9.40
CrO_3									16.77	28.20
F	n.a.	n.a.	n.a.	n.a.	2.39	3.16	n.a.	n.a.	n.a.	n.a.
Sum	100.20	98.79	100.31	99.85	100.82	101.75	100.23	99.76	99.86	100.03
Formula based on	5 cations				10 cat in Ca site		3 cat	2 cat		
	7 oxygens		4 oxy	4 oxy					4 oxy	4 oxy
Si	1.03	1.03	0.94	0.83	0.55	1.04		0.08		
Al	1.80	1.57	0.00	0.00			0.14	0.05		
Ti	0.00	0.00					0.00	0.56		
Zr+Nb								0.01		
Cr^{3+}							0.01	0.00		
Fe^{3+}	0.15	0.37					1.85	0.30		
Fe^{2+}	0.01	0.01	0.00	0.01	0.03	0.05	0.04		0.00	0.00
Ni+Zn+Cu							0.04			
Mn	0.00	0.00					0.01	0.00		
Mg	0.02	0.02	0.00	0.00			0.85	0.00		
Ca+Sr	2.00	2.00	1.94	1.83	9.97	9.95	0.05	1.00	0.05	0.03
Ba									1.00	0.99
Na	0.00	0.00	0.04	0.05						
K	0.00	0.00	0.02	0.09						
P^{5+}			0.05	0.17	5.31	4.12				
V^{5+}					0.06	0.06				
S^{6+}					0.10	0.78			0.58	0.29
Cr^{6+}									0.41	0.70
F					1.26	1.66				

Cl is below detection limit (<0.005 wt.%). n.a.—not analyzed; n.d.—not detected. FeO and Fe_2O_3 are calculated on charge balance.

Table 2. Reflectance values for nataliakulikite.

λ (nm)	**R_{max}/R_{min}**	**λ (nm)**	**R_{max}/R_{min}**
400	16.70/16.34	560	13.36/13.34
420	14.79/14.41	580	13.25/13.22
440	14.23/14.06	589 (COM)	13.20/13.15
460	14.17/14.09	600	13.13/13.09
470 (COM)	14.15/14.08	620	13.05/12.97
480	14.03/14.02	640	12.99/12.90
500	13.86/13.85	650 (COM)	12.98/12.83
520	13.69/13.68	660	12.90/12.78
540	13.48/13.48	680	12.78/12.64
546 (COM)	13.45/13.43	700	12.70/12.52

Larnite, gehlenite, and magnesioferrite occur as inclusions in nataliakulikite (Figures 4–6). This phase is commonly homogeneous, but rarely shows zoning or overgrows the Fe-rich perovskite cores (Figure 5). There is no obvious difference between two perovskite phases in both transmitted and reflected light. Moreover, they are also hardly distinguished on BSE images.

6. Chemical Composition of Nataliakulikite

The averaged empirical formula of nataliakulikite (based on 8 cations and 11 oxygens, EMPA-WDS, n = 47) is $(Ca_{3.992}Sr_{0.014}U_{0.004})_{4.010}(Ti_{1.933}Zr_{0.030}Nb_{0.002})_{1.965}(Fe^{3+}{}_{0.610}Fe^{2+}{}_{0.405}Cr_{0.005}Mn_{0.005})_{1.025}(Si_{0.447}Fe^{3+}{}_{0.337}Al_{0.216})_{1.000}O_{11}$ and shows the predominance Si in tetrahedral site (Table 3). In general, individual grains are commonly homogeneous in composition and rarely show chemical zoning (Figure 6). Although, different grains strongly vary in the content of Ti, Si, and Fe (Figure 7). The Ti content shows pronounced positive correlation with that of Fe^{2+} + Mn^{2+} and Zr + Nb and negative correlation with Si and Fe^{3+}. All these indicate two possible isomorphic schemes: $2\,^{VI}Fe^{3+} \leftrightarrow {}^{VI}Ti^{4+} + {}^{VI}Fe^{2+}$ and $^{IV}Fe^{3+} + 2\,^{VI}Ti^{4+} + {}^{VI}Fe^{2+} \leftrightarrow {}^{IV}Si^{4+} + 3\,^{VI}Fe^{3+}$.

Table 3. Chemical composition (WDS, wt.%) of nataliakulikite from larnite-gehlenite rock (W11-3), Nahal Morag Canyon, Hatrurim Basin, Israel.

Component	Nataliakulikite				Ntk-TEM	Ntk-1	Ntk-2	Ideal-1	Ideal-2
	n = 47	sd	min	max	n = 2	n = 5	n = 6		
SiO_2	5.05	0.63	3.71	6.87	5.11	5.11	5.17		4.53
TiO_2	29.04	1.71	25.48	32.64	29.51	29.69	29.44	29.38	30.14
ZrO_2	0.68	0.07	0.53	0.84	0.71	0.75	0.69		
Nb_2O_5	0.04	0.02	0.00	0.10	0.03	0.04	0.04		
Cr_2O_3	0.08	0.02	0.04	0.17	0.09	0.08	0.08		
Al_2O_3	2.07	0.41	1.24	3.02	2.14	2.37	2.47		1.92
Fe_2O_3	14.23	2.52	9.24	19.62	13.17	12.56	12.76	29.37	15.07
FeO	5.47	1.15	2.75	8.07	6.18	6.29	6.01	0.00	5.42
MnO	0.07	0.06	0.00	0.25	0.04	0.05	0.14		
CaO	42.10	0.16	41.82	42.50	42.01	42.11	42.09	41.25	42.37
SrO	0.27	0.04	0.20	0.34	0.24	0.31	0.32		
UO_2	0.20	0.07	0.07	0.33	0.13	0.28	0.28		
Sum	99.30				99.36	99.63	99.47	100.00	99.45
Formula based on 8 cations and 11 oxygens									
Si	0.447				0.451	0.450	0.456		0.400
Al	0.216				0.223	0.247	0.256		0.200
Fe^{3+}	0.338				0.325	0.303	0.288	1.000	0.400
Sum T	1.000				1.000	1.000	1.000	1.000	1.000
Ti	1.933				1.961	1.967	1.953	2.000	2.000
Zr+Nb	0.031				0.032	0.034	0.031		
Cr	0.006				0.006	0.006	0.006		
Fe^{3+}	0.610				0.551	0.530	0.559	1.000	0.600
Fe^{2+}	0.405				0.456	0.463	0.443	0.000	0.400
Mn	0.005				0.003	0.004	0.010		
Sum B	2.990				3.009	3.003	3.001	3.000	3.000
Ca	3.992				3.977	3.976	3.977	4.000	4.000
Sr	0.014				0.012	0.016	0.016		
U	0.004				0.003	0.005	0.005		
Sum A	4.010				3.991	3.997	3.999	4.000	4.000
End-members (mol.%)									
$Ca_4Ti_2Fe^{3+}Fe^{3+}O_{11}$	33.75				32.53	30.30	28.81	100.00	40.00
$Ca_4Ti_2Fe^{3+}AlO_{11}$	21.59				22.32	24.65	25.64	0.00	20.00
$Ca_4Ti_2Fe^{2+}SiO_{11}$	44.66				45.15	45.04	45.55	0.00	40.00

MgO, CuO, NiO, and ZnO are below detection limits (<0.005 wt.%). Ntk-TEM—nataliakulite grain used for high-resolution transmission electron microscopy (HRTEM) study (see Figure 9); Ntk-1-2—nataliakulite grains used for EBSD and Raman studies (see Figures 10 and 11); Ideal-1—$Ca_4Ti_2Fe^{3+}Fe^{3+}O_{11}$ and Ideal-2—$Ca_4Ti_2(Fe^{3+}{}_{0.6}Fe^{2+}{}_{0.4})(Fe^{3+}{}_{0.4}Si_{0.4}Al_{0.2})O_{11}$. FeO and Fe_2O_3 are calculated on charge balance.

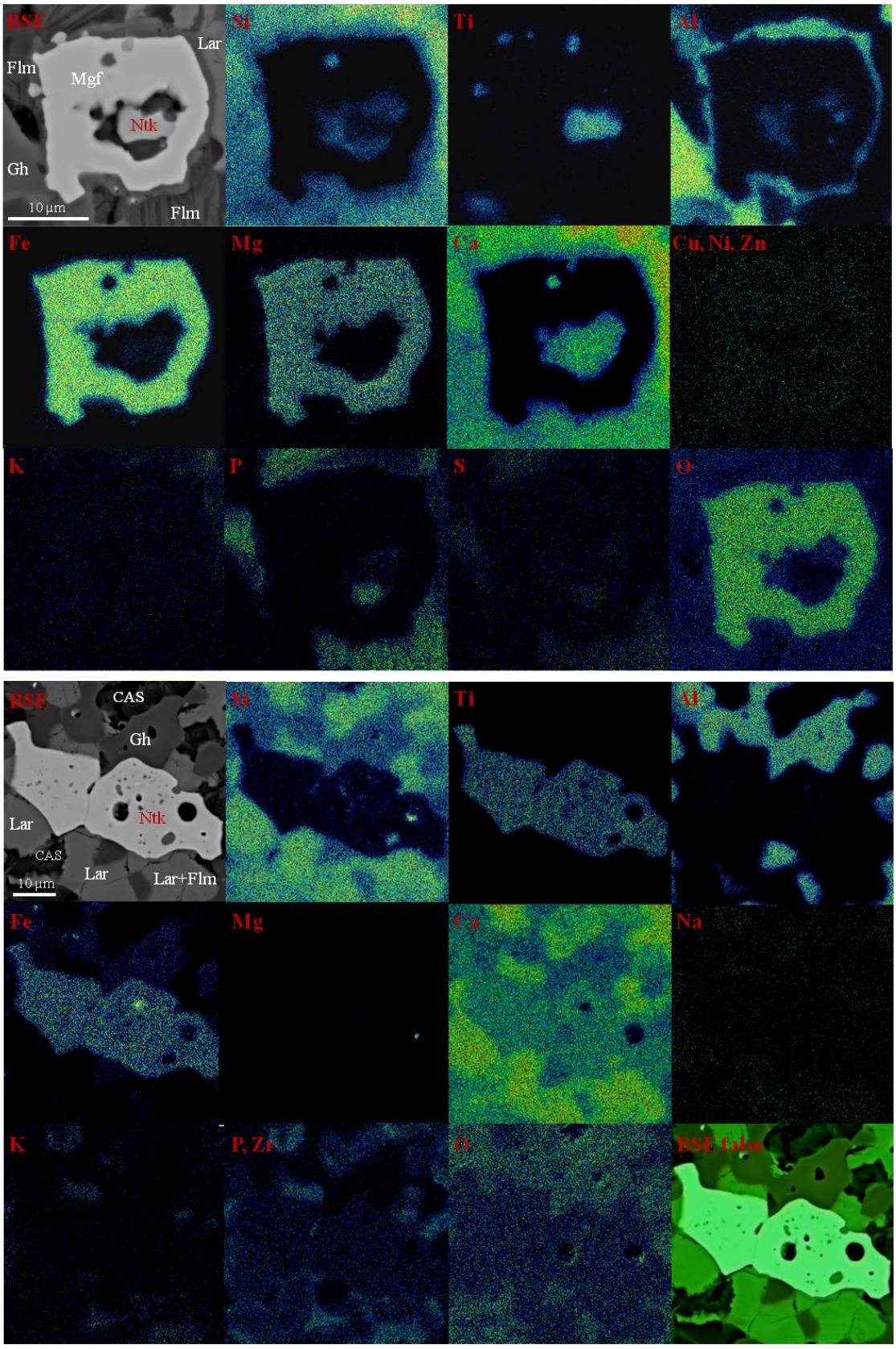

Figure 6. Elemental maps for nataliakulikite in larnite-gehlenite rock (holotype sample, W11-3) from Nahal Morag Canyon, Hatrurim Basin, Israel. Ntk—nataliakulikite; Mgf—magnesioferrite; Lar—larnite; Flm—flamite; Gh—gehlenite; CAS—hydrated Ca-silicates.

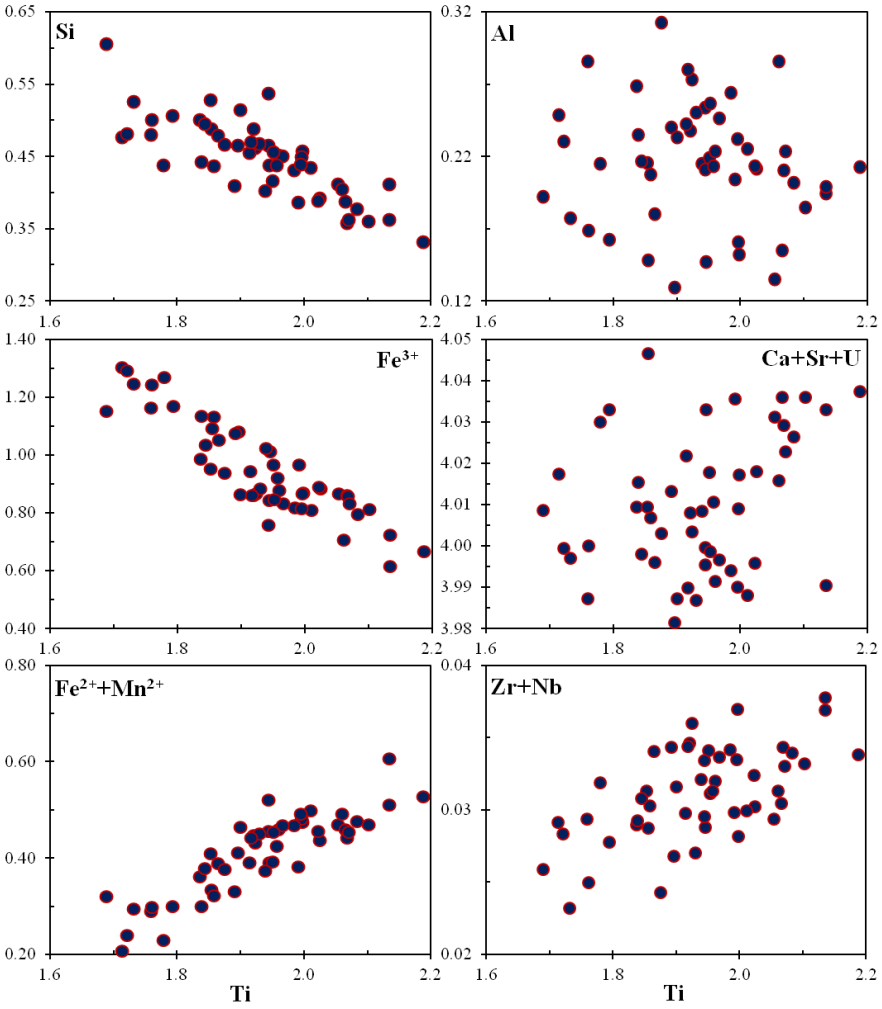

Figure 7. Chemical variations of Ti versus other elements (in apfu) for nataliakulikite.

In general, the composition of nataliakulikite changes from $Ca_{4.00}Ti_{1.72}(Fe^{3+}{}_{0.96}Fe^{2+}{}_{0.32})_{1.28}(Si_{0.61}Fe^{3+}{}_{0.20}Al_{0.19})_{1.00}O_{11}$ to $Ca_{4.00}Ti_{2.25}(Fe^{3+}{}_{0.22}Fe^{2+}{}_{0.53})_{0.75}(Si_{0.33}Fe^{3+}{}_{0.46}Al_{0.21})_{1.00}O_{11}$ (Figure 7). The mineral chemistry database is given in Table S1 (Supplementary materials). The simplified formula of nataliakulikite may be presented as $Ca_4Ti_2(Fe^{3+},Fe^{2+})(Si,Fe^{3+},Al)O_{11}$. However, according to the IMA-CNMNCC dominant-valency rule [77] the ideal formula should be given as $Ca_4Ti_2Fe^{3+}Fe^{3+}O_{11}$ or $Ca_4Ti_2Fe^{3+}{}_2O_{11}$ because the Si content is low in some grains and total $(Fe,Al)^{3+}$ is commonly higher than Si^{4+} in tetrahedral sites. Moreover, its ideal formula is equal to synthetic $Ca_4Ti_2Fe^{3+}{}_2O_{11}$ [8,9] and nataliakulikite may be considered as a Si-Fe^{2+}-rich natural equivalent of the synthetic phase ($2CaTiO_3{\cdot}Ca_2Fe^{3+}{}_2O_5$ in simplified form). General variations may be expressed in hypothetical end-members as (in mol.%): 20.3–45.8 $Ca_4Ti_2Fe^{3+}Fe^{3+}O_{11}$; 12.9–28.6 $Ca_4Ti_2Fe^{3+}AlO_{11}$; 33.1–60.6 $Ca_4Ti_2Fe^{2+}SiO_{11}$.

The impurities of Si and Fe^{2+} in nataliakulikite seem to stabilize its structure and prevent its decay into two perovskite phases (intergrowths/domains of $Ca_4Ti_2Fe_2O_{11}$ + Fe^{3+}-perovskite or $Ca_3TiFe_2O_8$ + $Ca_4Ti_2Fe_2O_{11}$). Some nataliakulikites in the holotype larnite-gehlenite sample (W11-3) grow over rare grains of Fe^{3+}-rich perovskite, which is compositionally close to $CaTi_{0.6}Fe^{3+}{}_{0.4}O_{2.8}$, x = 0.2, or ideally $Ca_5Ti_3Fe^{3+}{}_2O_{14}$ (Figure 5; Table 1 and Table S2). The nataliakulikite-Fe^{3+}-rich perovskite assemblage has never been reported before from the Hatrurim Basin. Previously one mineral of the perovskite-brownmillerite series (Fe-rich perovskite, shulamitite, sharyginite, brownmillerite) or two minerals: brownmillerite + shulamitite (or sharyginite), Fe-rich perovskite + shulamitite (or sharyginite) were indicated in the different larnite rocks [1,5,26,28,30,73].

7. Crystal Structure Data for Nataliakulikite

It was difficult to obtain single-crystal and X-ray powder diffraction data for nataliakulikite because of its very small crystal size (<10 μm), and its mineral structure was resolved by alternative methods (EBSD, HRTEM, and Raman spectroscopy). Before considering the structure of nataliakulikite, it is pertinent to dwell upon the structure of the $Ca_4Ti_2Fe_2O_{11}$ synthetic phase.

7.1. The Crystal Structure of Synthetic $Ca_4Ti_2Fe_2O_{11}$

The crystal structure of a perovskite-related synthetic oxide with a composition $Ca_4Ti_2Fe_2O_{11}$ has been studied in 1980× using X-ray diffraction and electron microscopy [8,9]. Initially Gonzáles-Calbet and Valet-Regí [8] suggested the following parameters of the phase: orthorhombic symmetry; *Pnma* or $Pn2_1a$ space group, a = 5.437(1) Å, b = 30.22(1) Å, c = 5.489(1) Å, V = 901.9(3) Å^3. The structural model was based on a stacking sequence of … OOOTOOOT′ … along the b axis. A more detailed refinement of the crystal structure of $Ca_4Ti_2Fe_2O_{11}$ has been done by high-resolution electron microscopy and crystallographic image processing (CIP) [9]: the space group is *Pnma*; the structure is composed of MeO_6 octahedra and MeO_4 tetrahedra, arranged as … OOOTOOOT … sequence along the long b-axis. The crystal structure of synthetic $Ca_4Ti_2Fe_2O_{11}$ is shown in Figure 8.

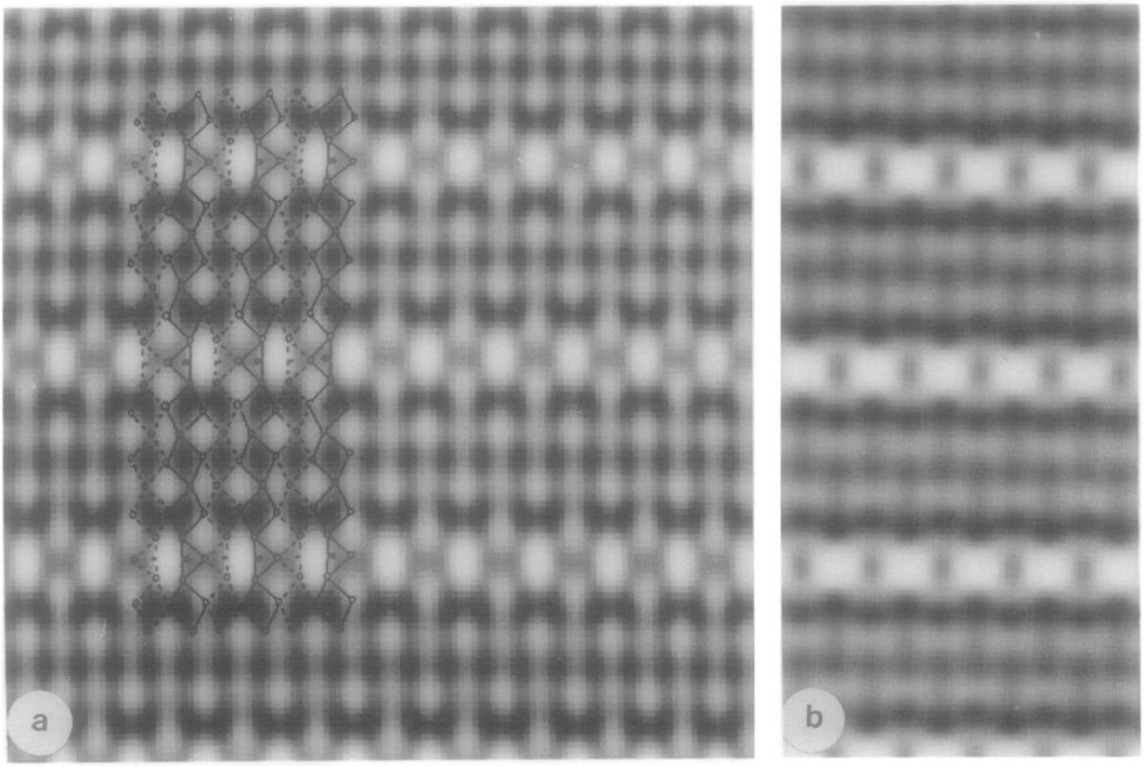

Figure 8. The crystal structure of synthetic $Ca_4Ti_2Fe_2O_{11}$ (Figure 4 in [9]). Its structure projected down the a-axis, after applying CIP on the HRTEM. The phase used in (**a**) is the symmetrical phase. The same data was used in (**b**), except that the phase of the (002) reflection was reversed; i.e., 0″ instead of 180″ as in (**a**). The structural model of $Ca_4Ti_2Fe_2O_{11}$ is overlaid on the correct structure seen in (**a**).

7.2. HRTEM Data for Nataliakulikite

The unit cell parameters of nataliakulikite were calculated from HRTEM data obtained from FIB-milled foil (Figure 9). They are: a = 5.254 Å; b = 30.302 Å; c = 5.488 Å; V = 873.7 Å^3; Z = 4; orthorhombic symmetry. Suggested space group is *Pnma (*no. 62) according to [9]. Additionally, the dark and bright field images and SAED reveal that nataliakulikite is a homogeneous phase, and no striking, twining, oriented intergrowths, or different stacking were indicated in its crystal structure.

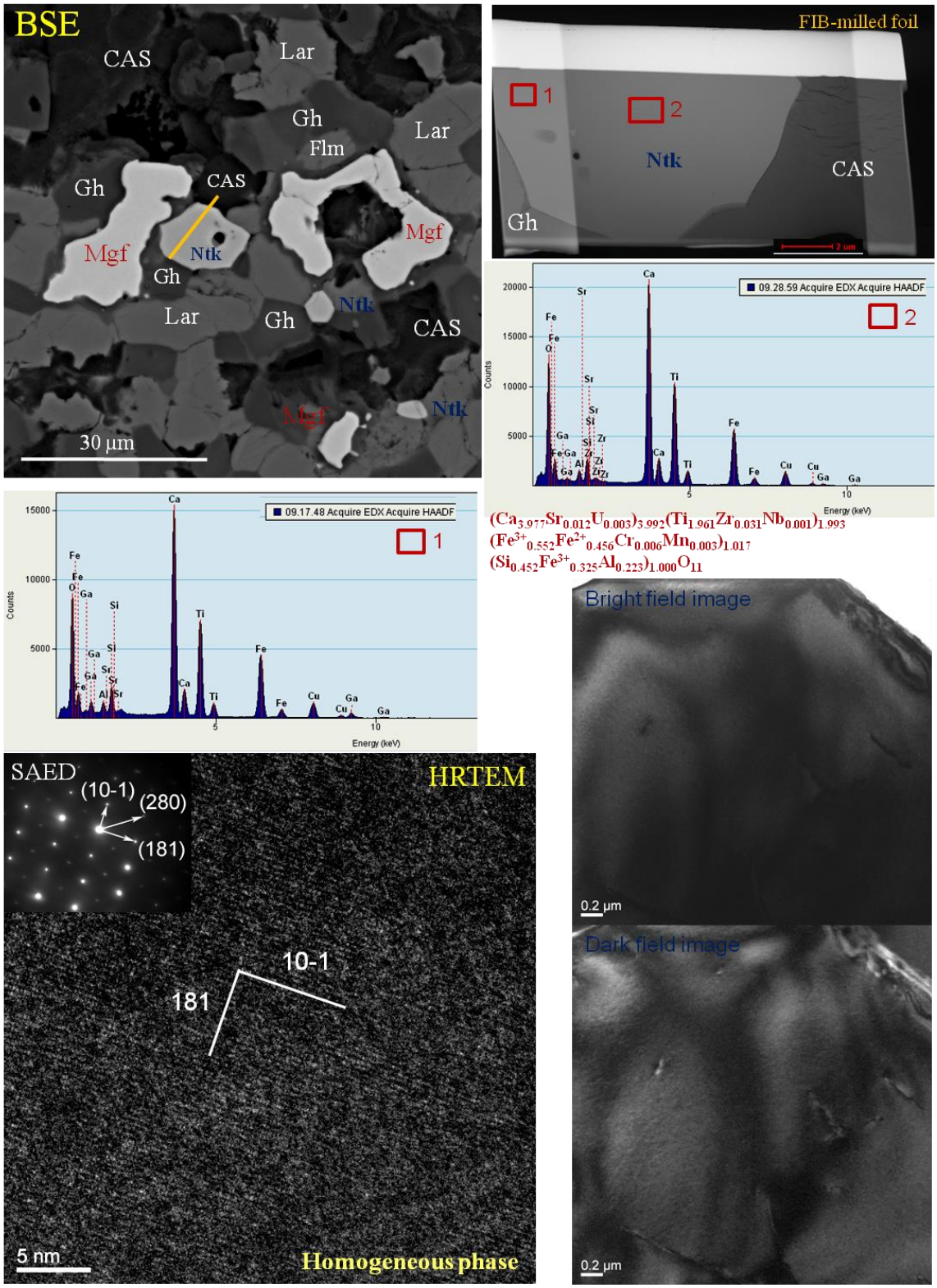

Figure 9. High-resolution transmission electron microscopy (HRTEM) data for nataliakulikite in larnite-gehlenite rock (holotype sample, W11-3) from Nahal Morag Canyon, Hatrurim Basin, Israel. Ntk—nataliakulikite; Mgf—magnesioferrite; Lar—larnite; Flm—flamite; Gh—gehlenite; CAS—hydrated Ca-silicates. No striking, twining, oriented intergrowths or different stacking were indicated.

The theoretical powder diffraction pattern was calculated using the unit cell dimensions obtained by HRTEM, structural model for $Ca_4Ti_2Fe_2O_{11}$ [9], and the empirical formula of nataliakulikite. Data for nataliakulikite (Cu$K\alpha_1$ = 1.540598 Å, Bragg-Brentano geometry, fixed slit, no anomalous dispersion, $I > 1$) are compared in Table 4 with those for synthetic $Ca_4Ti_2Fe_2O_{11}$ [8,9].

Table 4. Calculated powder diffraction data for nataliakulikite and synthetic $Ca_4Ti_2Fe_2O_{11}$ (Cu$K\alpha_1$ = 1.540598 Å, Bregg-Brentano geometry, $I > 1$; data were calculated using PowderCell 2.4 [78]).

			Nataliakulikite		**Synthetic [8,9]**	
h	***k***	***l***	$d_{calc,}$ **Å**	I_{rel}	$d_{calc,}$ **Å**	I_{rel}
0	**2**	**0**	**15.151**	**19**	**15.110**	**18**
0	4	0	7.576	5	7.555	5
0	6	0	5.050	1	5.037	1
0	3	1	4.822	6	4.820	6
0	5	1	4.068	7	4.063	7
1	**0**	**1**	**3.795**	**8**	**3.863**	**9**
0	8	0	3.788	4	3.778	4
1	2	1	3.681	1	3.742	1
1	3	1	3.553	3	3.607	3
0	7	1	3.399	2	3.393	2
1	4	1	3.393	1		
1	5	1	3.217	1	3.255	1
0	9	1	2.870	4	2.864	4
0	**0**	**2**	**2.744**	**23**	**2.745**	**22**
1	**8**	**1**	**2.681**	**100**	**2.701**	**100**
2	**0**	**0**	**2.627**	**26**	**2.719**	**28**
2	1	0	2.617	1	2.708	1
2	3	0	2.542	2	2.625	2
1	0	2	2.432	1	2.450	1
1	3	2	2.365	5	2.381	5
0	8	2	2.222	6	2.220	6
2	8	0	2.159	4	2.207	4
0	13	1	2.145	1	2.141	1
1	7	2	2.121	1	2.131	1
1	8	2	2.047	1	2.056	1
2	8	1	2.009	2	2.047	2
2	**0**	**2**	**1.898**	**30**	**1.931**	**31**
0	**16**	**0**	**1.894**	**22**	**1.889**	**21**
2	5	2	1.811	1	1.840	1
1	13	2	1.683	1	1.686	1
3	0	1	1.668	1	1.721	2
3	3	1	1.646	1	1.696	1
3	5	1	1.609	1	1.655	1
1	**8**	**3**	**1.572**	**14**	**1.576**	**13**
3	8	1			1.566	10
0	16	2	1.559	5	1.556	5
2	16	0			1.551	6

The strongest diffraction lines are given in bold.

7.3. EBSD Data for Nataliakulikite

The additional structural data were obtained using the EBSD technique (Figure 10) and fitted to the structural model of synthetic $Ca_4Ti_2Fe_2O_{11}$ [8,9]. Fitting of the EBSD patterns for a $Ca_4Ti_2Fe_2O_{11}$ model with the cell parameters [8,9] resulted in the parameter MAD = 0.18°–0.36° (best-good fit). The EBSD studies reveal structural identity of nataliakulikite and synthetic $Ca_4Ti_2Fe_2O_{11}$ compound.

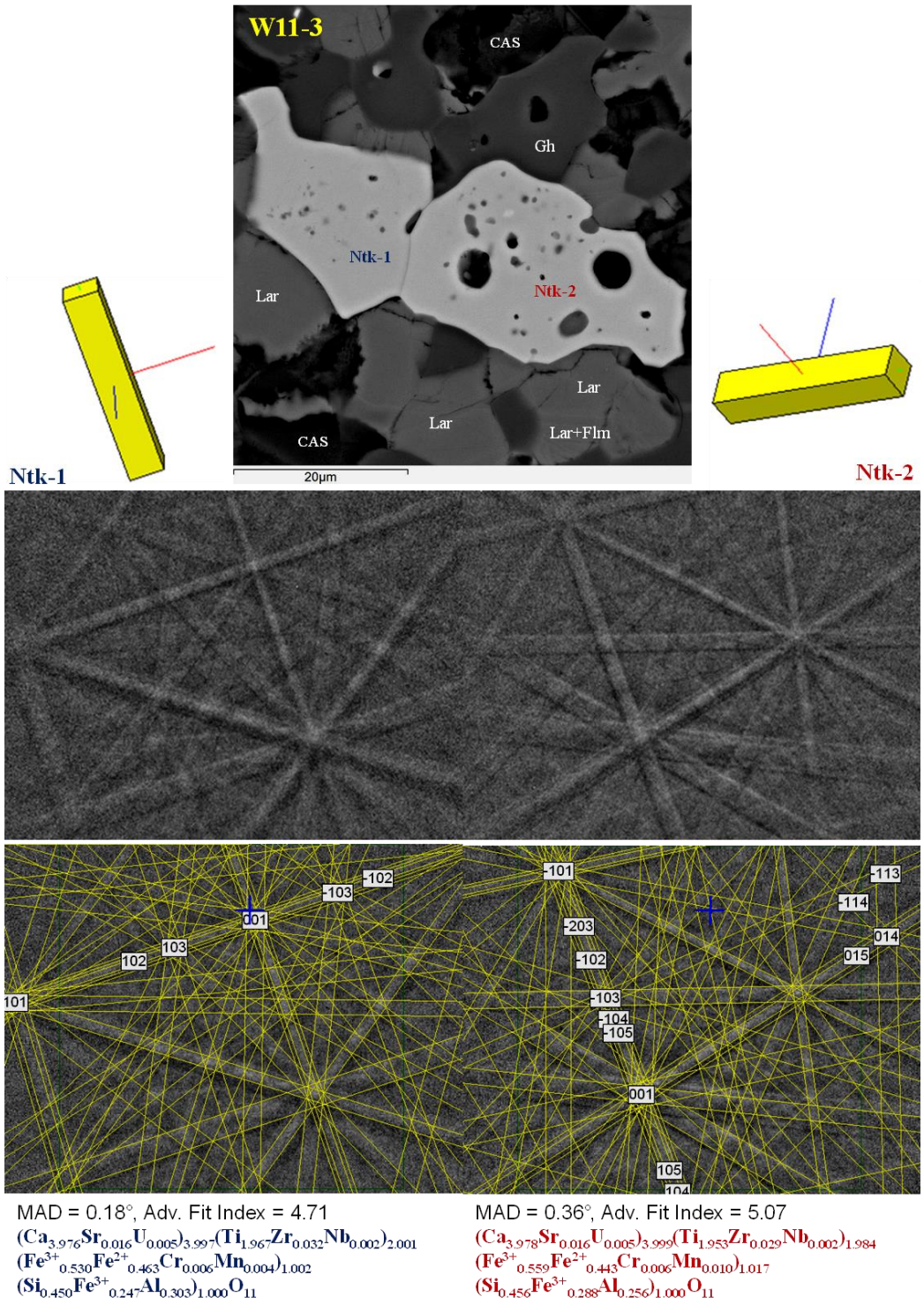

Figure 10. BSE image, crystal orientation, electron backscattered diffraction (EBSD) patterns, and the Kikuchi patterns and chemical composition for two grains of nataliakulikite (detector distance—15–20 mm), larnite-gehlenite rock (holotype sample, W11-3) from Nahal Morag Canyon, Hatrurim Basin, Israel.

7.4. Raman Spectroscopy for Nataliakulikite

Main Raman bands, which are characteristic for nataliakulikite, are (in cm^{-1}, Figure 11): 128, 223, 274, 468 (shoulder), 562, 790, 915 (shoulder), and 1450 (overtone). No bands have been detected in the 3000-4000 cm^{-1} region (main for OH vibrations). The Raman spectra for nataliakulikite are interpreted following the results for shulamitite and sharyginite [30,31]. Bands below 400 cm^{-1} are

ascribed to the polyhedral CaO_8 and octahedral $(Fe^{3+},Ti)O_6$ vibrations. Bands at 468 and 562 cm^{-1} are related to tetrahedral $(Fe^{3+},Si,Al)O_4$ bending vibrations ($\nu_4 + \nu_2$). The strongest band in the Raman spectra of nataliakulikite at 790 cm^{-1} represents symmetric stretching vibrations ν_1 of $(Fe^{3+},Si,Al)O_4$ tetrahedra. The broadening of the bands at 562 and 790 cm^{-1} may indicate disordering of Fe^{3+}, Si and Al in tetrahedral sites.

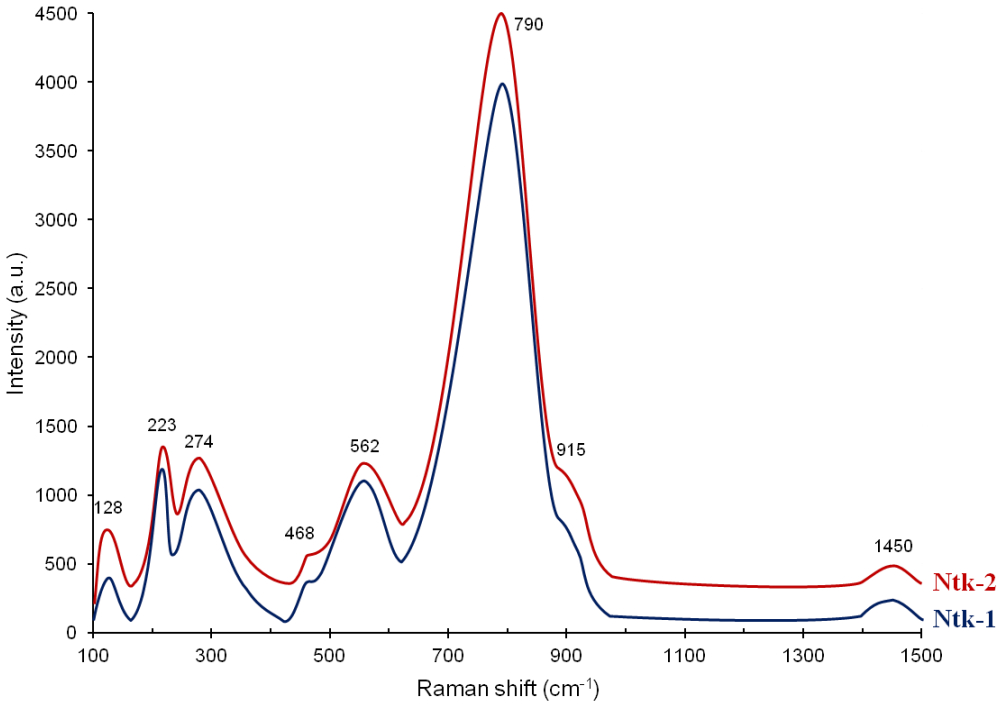

Figure 11. Raman spectra for two grains of nataliakulikite in larnite-gehlenite rock (holotype, W11-3) from Nahal Morag Canyon, Hatrurim Basin, Israel. Ntk-1, Ntk-2—see Figure 10.

8. Discussion

Composition and structural data obtained by HRTEM, EBSD, and Raman techniques remarkably show that nataliakulikite is a Si-Fe^{2+}-rich analogue of the synthetic phase $Ca_4Ti_2Fe_2O_{11}$ (*Pnma*, no. 62, [8,9]). It belongs to the perovskite-brownmillerite pseudobinary series with the generalized formula $CaTi_{1-2x}Fe_{2x}O_{3-x}$ ($0 \leq x \leq 0.5$) [6,8,10,20–22] and may be represented in the end members of this series as 66.66% $CaTiO_3$ and 33.33% $Ca_2Fe_2O_5$. All members of the series in accordance with the material science terminology [6–12] may be classified as "layered perovskites". According to the recent nomenclature of the perovskite supergroup [23] nataliakulikite belongs to the anion deficient perovskites (brownmillerite subgroup, non-stoichiometric perovskites group). The only difference between nataliakulikite and synthetic $Ca_4Ti_2Fe_2O_{11}$ phase is that the tetrahedral Fe^{3+} is partially substituted by Si and Al in the structure of natural mineral. No strict constraints on the order-disorder in the tetrahedral layer are available because the nataliakulikite grains were too small for structure refinement. Nevertheless, the Raman data indicate a possible disordering of Fe^{3+}, Si and Al in tetrahedra.

8.1. Phase Relations in the System Perovskite-Brownmillerite

The synthetic compounds of the $CaTiO_3$-$CaFe_2O_5$ series have been exhaustively covered by previous workers (since 1960–70s) due to specific properties of oxygen-deficient Fe-rich perovskites, such as superconductivity, oxygen ionic conductivity, as well as electronic conductivity. Numerous compounds, corresponding to the general formula $CaTi_{1-2x}Fe_{2x}O_{3-x}$ ($0 \leq x \leq 0.5$), were synthesized within this system [6]. However, only four orthorhombic compounds are fully ordered in oxygen

vacancies and seem to be most stable: $CaTiO_3$ (x = 0), $Ca_4Ti_2Fe_2O_{11}$ (x = 0.25), $Ca_3TiFe_2O_8$ (x = 0.33) and $Ca_2Fe_2O_5$ (x = 0.5) [6–8,10–12,20–22,79]. According to the phase diagram $CaTiO_3$–$CaFeO_{2.5}$ (Figure 12), the coexistence of perovskite and brownmillerite is impossible in any associations, because phases $Ca_3TiFe_2O_8$ and $Ca_4Ti_2Fe_2O_{11}$ are more stable in energy than the perovskite + brownmillerite paragenesis [79]. The $Ca_4Ti_2Fe_2O_{11}$ phase seems not to be in association with $Ca_2Fe_2O_5$; it transforms into $Ca_3TiFe_2O_8$ or $Ca_3TiFe_2O_8$ + $Ca_2Fe_2O_5$. The intermediate phases $Ca_4Ti_2Fe_2O_{11}$ and $Ca_3TiFe_2O_8$ should be stoichiometric in composition without vacancies of cations and oxygen. Any deviations in Ti content should lead to the appearance of nanoscale intergrowths/domains of $Ca_4Ti_2Fe_2O_{11}$ + Fe-perovskite, $Ca_3TiFe_2O_8$ + $Ca_4Ti_2Fe_2O_{11}$ or $Ca_3TiFe_2O_8$ + $Ca_2Fe_2O_5$. In addition to these four compounds, the ordered $Ca_5TiFe_4O_{13}$ occurs in the $Ca_3TiFe_2O_8$ - $Ca_2Fe_2O_5$ region [13].

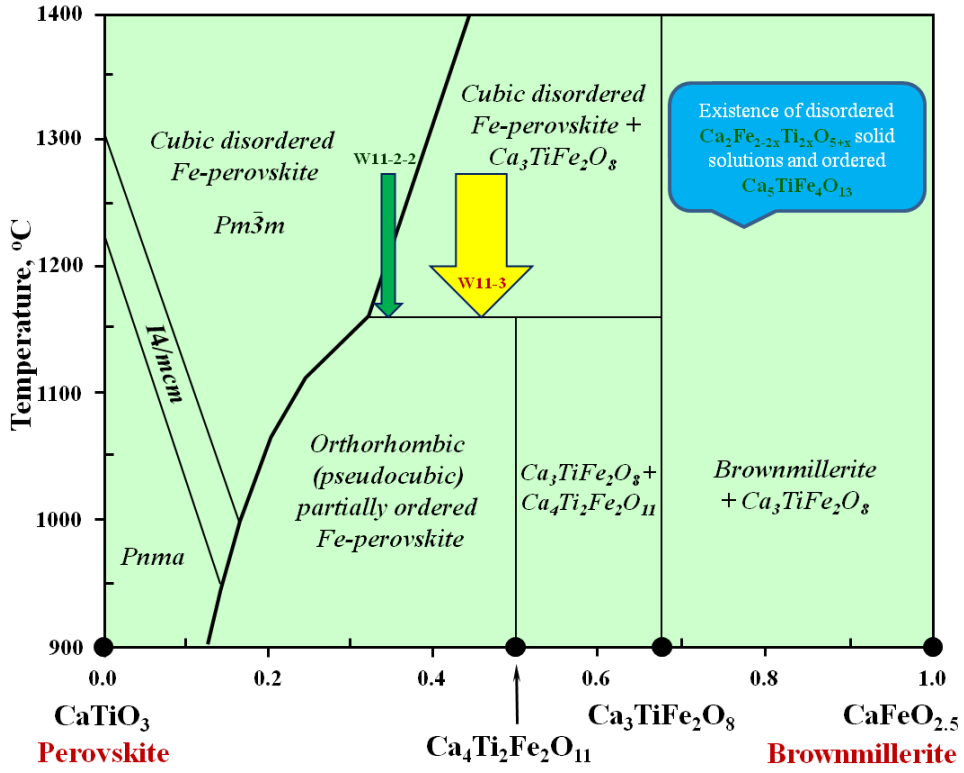

Figure 12. Phase diagram for the system $CaTiO_3$-$CaFeO_{2.5}$ modified after [13,20–22]. Arrows show the possible ways for the formation of the assemblages of Fe^{3+}-rich perovskite with nataliakulikite (W11-3) and with sharyginite (W11-2-2) during cooling (larnite-gehlenite rocks, Nahal Morag Canyon, Hatrurim Basin, Israel). See Table S2 (Supplementary materials) for mineral chemistry of Fe^{3+}-perovskite.

8.2. Natural Equivalents for Phases of the Perovskite-Brownmillerite Series

At present, all key ordered compounds on the phase diagram $CaTiO_3$-$CaFe_2O_5$ [13,20–22] have been found as minerals in natural combustion metamorphism environments (mainly in Ca-rich metacarbonate rocks). Nataliakulikite was the latest mineral in the system discovered in natural occurrence. The natural phases close to synthetic $Ca_5TiFe^{3+}{}_4O_{13}$-$Ca_5TiFe^{3+}{}_2Al_2O_{13}$ [13] were previously chemically described in some rocks [26,80,81], but they are not yet approved by the CNMNC IMA as a new mineral species. The perovskite - brownmillerite series now includes perovskite and Fe^{3+}-perovskite $CaTiO_3$-$CaTi_{1-2x}Fe_{2x}O_{3-x}$ ($0 \leq x \leq 0.4$), brownmillerite $Ca_2Fe^{3+}AlO_5$, srebrodolskite $Ca_2Fe^{3+}Fe^{3+}O_5$, shulamitite $Ca_3TiFe^{3+}AlO_8$, sharyginite $Ca_3TiFe^{3+}{}_2O_8$ and nataliakulikite $Ca_4Ti_2(Fe^{3+},Fe^{2+})(Si,Fe^{3+},Al)O_{11}$ [18,19,24–31]. In addition, according natural observations and experimental data, the following solid solutions towards Al-rich compositions are well identified: srebrodolskite-brownmillerite $Ca_2Fe^{3+}Fe^{3+}O_5$-$Ca_2Fe^{3+}AlO_5$; sharyginite-shulamitite $Ca_3TiFe^{3+}Fe^{3+}O_8$-$Ca_3TiFe^{3+}AlO_8$, individual members of which are subdivided due to structural

phase transition and the Fe^{3+} ↔ Al substitution in tetrahedral sites [26,28–31,82–84]. The same solid solutions may exist for both nataliakulikite line $Ca_4Ti_2Fe^{3+}Fe^{3+}O_{11}$-$Ca_4Ti_2Fe^{3+}AlO_{11}$ and line $Ca_5TiFe^{3+}{}_2Fe^{3+}{}_2O_{13}$-$Ca_5TiFe^{3+}{}_2Al_2O_{13}$ [5]. Surprisingly, the Hatrurim Basin is now sole CM outcrop, where all members of the perovskite-brownmillerite series have been found. The general structural data for all these minerals are summarized in Table 5.

Table 5. Structural data for ordered phases (natural and synthetic) of the perovskite-brownmillerite pseudobinary series.

Mineral	Perovskite	Natalia-kulikite	Sharyginite	Shulamitite	Synthetic phase	Srebrodol-skite	Brown-millerite
Formula	$CaTiO_3$	$Ca_4Ti_2Fe^{3+}Fe^{3+}O_{11}$	$Ca_3TiFe^{3+}Fe^{3+}O_8$	$Ca_3TiFe^{3+}AlO_8$	$Ca_5TiFe^{3+}{}_2Al_2O_{13}$	$Ca_2Fe^{3+}Fe^{3+}O_5$	$Ca_2Fe^{3+}AlO_5$
Orthorhombic space group	*Pnma*	*Pnma*	$P2_1ma$	*Pmma*	*Body-centered*	*Pnma*	*I2mb*
Unit cell:							
a, Å	5.544	5.254	5.423(2)	5.4200(6)		5.420(3)	5.57
b, Å	7.6412	30.302	11.150(8)	11.064(1)	18.6	14.752(3)	14.52
c, Å	5.381	5.488	5.528(2)	5.5383(7)		5.594(3)	5.34
V, $Å^3$	223.8	873.7	334.3(3)	332.12		447.27	431.88
Z	4	4	2	2		4	4
Sequence	OOOOOO	OOTOOO	OTOOTO	OT′OOT′O	OTOTOO	OTOT′OT	OTOTOT
Density (g/cm^3)	4.04	4.006	3.943	3.84		3.94	3.74
Reference	[21]	This study; [8,9]	[31]	[30]	[13]	[25,83]	[24,83]

O, T—octahedral and tetrahedral layers. T, T′—different stacking sequence of tetrahedral chains.

The natural relations among minerals of the perovskite-brownmillerite series also do not contradict the phase diagram $CaTiO_3$-$CaFe_2O_5$ [20–22]. Different types of Ca-rich assemblages in the Hatrurim Basin and other CM outcrops worldwide may contain a single mineral of the series (usually brownmillerite, rarely shulamitite or sharyginite), or two such minerals (brownmillerite/srebrodolskite + shulamitite/sharyginite, Fe-rich perovskite + shulamitite/sharyginite, Fe-rich perovskite + nataliakulikite) [18,19,24–31]. The "prohibited" associations of Fe-rich perovskite + brownmillerite and nataliakulikite + brownmillerite were not observed in any CM rocks. Although, individual grains of perovskite and brownmillerite may occur in some rock samples. The triple Fe-rich perovskite + shulamitite/sharyginite + brownmillerite/srebrodolskite assemblage was found only in metacarbonate xenoliths of the Bellerberg volcano, Germany [28–30], but in this case there is no contradiction with the phase diagram $CaTiO_3$-$CaFe_2O_5$ because perovskite and brownmillerite have no immediate contacts.

Assuming the $CaTiO_3$-$Ca_2Fe_2O_5$ phase diagram (Figure 12), the phase $Ca_4Ti_2Fe_2O_{11}$ (synthetic Fe^{3+}-dominant analog of nataliakulikite [8,9]) should be stoichiometric without vacancies of cations and oxygen. Any deviations from Ti = 2 (apfu) should lead to intergrowths/domains of either $Ca_4Ti_2Fe_2O_{11}$ + $Ca_3TiFe_2O_8$ or $Ca_4Ti_2Fe_2O_{11}$ + Fe^{3+}-perovskite. The holotype nataliakulikite is very close to stoichiometric composition in respect to the Ti content (Table 3, Figure 7). HRTEM study reveals that holotype nataliakulikite is structurally homogeneous and does not contain any domains and intergrowths (Figure 9). It is different from the synthetic compound $Ca_4Ti_2Fe_2O_{11}$ in both high silica and alumina contents, and by believable disordering of Fe^{3+}, Al^{3+}, and Si^{4+} in tetrahedral sites, and the appearance of Fe^{2+} in octahedral sites. The impurities of Si and Fe^{2+} in nataliakulikite seem to stabilize its structure and prevent its decay into two perovskite phases (intergrowths/domains of $Ca_4Ti_2Fe_2O_{11}$ + Fe^{3+}-perovskite or $Ca_3TiFe_2O_8$ + $Ca_4Ti_2Fe_2O_{11}$).

The nature of Si-enrichment of nataliakulikite, and related Fe-perovskite in the studied larnite-gehlenite rock, remains unclear. Possibly it deals with nano-sized inclusions of Ca-silicates in these phases. On other hand, it may be related to high Si activity at high-temperature formation of the rock. Note that SiO_2 does not exceed 3 wt.% in other minerals of the perovskite-brownmillerite series in the Hatrurim Basin larnite and larnite-gehlenite rocks [5,26,30,73]. However, some synthetic

phases and minerals in high-temperature Ca-rich paralavas may be extremely rich in SiO_2 (up to 11 wt.%) [80,81,85].

8.3. Temperature Estimation for Nataliakulikite at the Hatrurim Basin

The formation temperature of the Fe-perovskite + shulamitite/sharyginite assemblage from the Hatrurim Basin larnite-mayenite rock was reconstructed previously using the $CaTiO_3$-$Ca_2Fe_2O_5$ phase diagram, and the assemblage was found out to be stable at >1160 °C [26]. The minimum temperature of its formation was estimated to be 1170–1200 °C proceeding from the Fe-perovskite composition and the modal proportion of phases in the rock [26]. Note that the presence of Al, Cr, and some other impurities in Fe-perovskite can lead to higher temperature estimates. The same assemblages in other CM rocks worldwide gave similar temperature values [28–31]. Moreover, the assemblage of Fe-perovskite + nataliakulikite is also applicable for estimation of formation temperatures of rocks [19].

The detailed petrography (larnite-flamite intergrowths, Fe-perovskite + nataliakulikite) has shown that studied larnite-gehlenite rock seems to be formed by high-temperature solid-phase reactions without any signs of melting. The presence of nataliakulikite in the rock indicates the upper temperature limit as 1160 °C, whereas chemical composition of Fe^{3+}-rich perovskite in association with nataliakulikite gave minimal temperature estimation >1160 °C (Figure 12). However, the true formation temperature may be higher because both perovskite and nataliakulikite are enriched in Si.

Additionally, we provided independent evaluation for the assemblage khesinite + Fe-perovskite + sharyginite from larnite-gehlenite pebble (Figure 13), which adjoins the nataliakulite-bearing ones in "pseudoconglomerate" layer at Nahal Morag Canyon. The presence of natural Ca-silicoferrite (khesinite) strongly suggests the upper temperature limit as 1220–1255 °C [86,87]. Whereas, perovskite composition in association with sharyginite gave a broader range (1200–1160 °C, Figure 12). In general, this estimation is very similar to that of previous data for the Hatrurim larnite rocks [26]. We can suggest that the temperature gradient for neighboring larnite-gehlenite pebbles, within "pseudoconglomerate" layer, at Nahal Morag Canyon, was very minimal and the difference in mineralogy of Ti-Fe-bearing assemblages seems to be related to composition of sedimentary protolith.

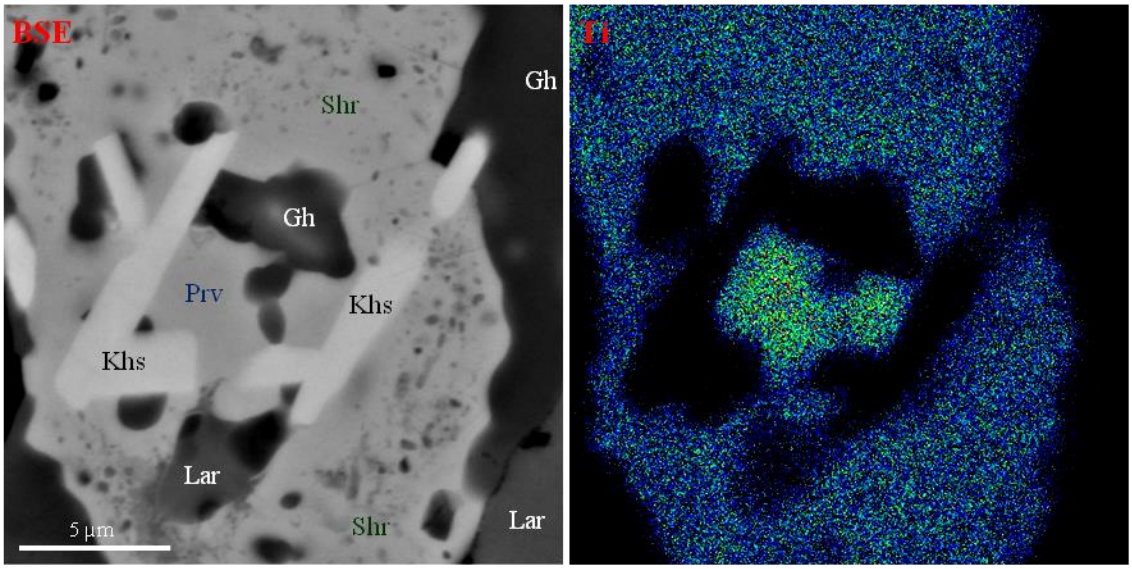

Figure 13. BSE image and elemental map of Ti for association khesinite + Fe^{3+}-perovskite + sharyginite in larnite-gehlenite rock (sample W11-2-2) from Nahal Morag Canyon, Hatrurim Basin, Israel. Khs—khesinite; Prv—Fe^{3+}-rich perovskite; Shr—sharyginite; Lar—larnite; Gh—gehlenite. Chemical composition of Fe^{3+}-perovskite is given in Table S2 (Supplementary materials).

9. Concluding Remarks

Thus, the detailed mineralogical and petrographic studies for larnite-gehlenite rocks at the Hatrurim Basin gave a possibility to describe physical properties, chemical composition and some structural affinities for a new mineral, nataliakulikite, $Ca_4Ti_2(Fe^{3+},Fe^{2+})(Si,Fe^{3+},Al)O_{11}$. On the basis of the dominant-valency rule [77] (R^{3+}-cations > Si^{4+} and Fe^{3+} > Al), the ideal formula should be $Ca_4Ti_2Fe^{3+}Fe^{3+}O_{11}$ or $Ca_4Ti_2Fe^{3+}{}_2O_{11}$. This mineral belongs to the perovskite supergroup (brownmillerite subgroup, non-stoichiometric perovskites group, anion deficient perovskites).

Assuming the $CaTiO_3$–$Ca_2Fe_2O_3$ phase diagram and in addition to the Fe-perovskite + sharyginite/shulamitite paragenesis [26], nataliakulikite and its association with Fe^{3+}-rich perovskite may be used as new thermometers for metacarbonate rocks of the high-temperature region of the spurrite-merwinite facies.

Supplementary Materials: The following are available online at http://www.mdpi.com/2075-163X/9/11/700/s1, Table S1: Chemical composition (WDS, wt.%) of nataliakulikite from larnite-gehlenite rock (W11-3), Nahal Morag Canyon, Hatrurim Basin, Israel; Table S2: Chemical composition (WDS-EDS, wt.%) of Fe^{3+}-rich perovskite from larnite-gehlenite rocks (W11-3, W11-2-2), Nahal Morag Canyon, Hatrurim Basin, Israel; Cif file: nataliakulikite.

Author Contributions: V.V.S. and E.V.S. wrote the paper. V.V.S. performed the mineralogical description, measurements of chemical composition, and Raman studies of nataliakulikite and related minerals. G.A.Y., R.W., E.N.N., N.S.K., Y.V.S., and L.A.P. provided EBSD, TEM, EMPA, SEM, structural and reflectance studies.

Funding: This research was funded by the Russian Science Foundation, grant number 17-17-01056. The field work and sample collection was partly supported the State assignment projects (IGM SD 0330-2016-0005, 0330-2016-0004).

Acknowledgments: The authors would like to thank M.V. Khlestov (IGM SD RAS) for technical assistance at SEM studies. Yevgeny Vapnik (Ben-Gurion University, Beer-Sheva, Israel) is thanked for providing of fruitful field trips in the Hatrurim Basin in 2004 and 2019. The last version of the manuscript was improved through comments and suggestions by T. Perepelova (IGM, Novosibirsk). We are highly appreciative of the valuable comments and suggestions of two anonymous reviewers.

Conflicts of Interest: The authors declare no conflict of interest.

References

1. Gross, S. The mineralogy of the Hatrurim Formation, Israel. *Geol. Surv. Isr. Bull.* **1977**, *70*, 80.
2. Burg, A.; Starinsky, A.; Bartov, Y.; Kolodny, Y. Geology of the Hatrurim Formation ("Mottled Zone") in the Hatrurim basin. *Isr. J. Earth Sci.* **1991**, *40*, 107–124.
3. Burg, A.; Kolodny, Y.; Lyakhovsky, V. Hatrurim-2000: The "Mottled Zone" revisited, forty years later. *Isr. J. Earth Sci.* **1999**, *48*, 209–223.
4. Novikov, I.; Vapnik, Y.; Safonova, I. Mud volcano origin of the Mottled Zone, South Levant. *Geosci. Front.* **2013**, *4*, 597–619. [CrossRef]
5. Sokol, E.V.; Kokh, S.N.; Sharygin, V.V.; Danilovsky, V.A.; Seryotkin, Y.V.; Liferovich, R.; Deviatiiarova, A.S.; Nigmatulina, E.N.; Karmanov, N.S. Mineralogical diversity of Ca_2SiO_4-bearing combustion metamorphic rocks in the Hatrurim Basin: Implications for storage and partitioning of elements in oil shale clinkering. *Minerals* **2019**, *9*, 465. [CrossRef]
6. Grenier, J.C.; Pouchard, M.; Hagenmuller, P. Vacancy ordering in oxygen-deficient perovskite-related ferrites. *Struct. Bond.* **1981**, *47*, 1–25. [CrossRef]
7. Causa, M.T.; Zysler, R.D.; Tovar, M.; Vallet-Regí, M.; González-Calbet, J.M. Magnetic properties of the $Ca_nFe_2Ti_{n-2}O_{3n-1}$ perovskite related series: An EPR study. *J. Solid State Chem.* **1992**, *98*, 25–32. [CrossRef]
8. Gonzáles-Calbet, J.M.; Valet-Regí, M. A new perovskite-type compound: $Ca_4Fe_2Ti_2O_{11}$. *J. Solid State Chem.* **1987**, *68*, 266–272. [CrossRef]
9. Hovmöller, S.; Zou, X.; Wang, D.N.; Gonzáles-Calbet, J.M.; Valet-Regí, M. Structure determination of $Ca_4Fe_2Ti_2O_{11}$ by electron microscopy and crystallographic image processing. *J. Solid State Chem.* **1988**, *77*, 316–321. [CrossRef]
10. Grenier, J.-C.; Darriet, J.; Pouchard, M.; Hagenmuller, P. Mise en evidence d'une nouvelle fammille de phases de type perovskite lacunaire ordonnee de formule $A_3M_3O_8$ ($AMO_{2.67}$). *Mater. Res. Bull.* **1976**, *11*, 1219–1226. [CrossRef]

11. Grenier, J.-C.; Schiffmacher, G.; Caro, P.; Pouchard, M.; Hagenmuller, P. Etude par diffraction X et microscopie electronique du système $CaTiO_3$-$CaFe_2O_5$. *J. Solid State Chem.* **1977**, *20*, 365–379. [CrossRef]
12. Rodrígues-Carvajal, J.; Valett-Regí, M.; González-Calbet, J.M. Perovskite threefold superlattices: A structure determination of the $A_3M_3O_8$ phase. *Mater. Res. Bull.* **1989**, *24*, 423–430. [CrossRef]
13. Marinho, M.B.; Glasser, F.P. Polymorphism and phase changes in the ferrite phase of cements induced by titanium substitution. *Cem. Concr. Res.* **1984**, *14*, 360–368. [CrossRef]
14. Melgunov, S.V.; Kulik, N.A.; Bakumenko, I.T. Mineralogy and geochemistry of metamorphogenic segregative pegmatoids. In *Proceedings of Institute of Geology and Geophysics*; Nauka: Novosibirs, Russia, 1975; Volume 236, p. 92. (In Russian)
15. Derevianko, A.P.; Markin, S.V.; Kulik, N.A.; Kolobova, K.A. Lithic raw material exploitation in the Sibiryachikha facies, the Middle Paleolithic of Altai. *Archaeol. Ethnol. Anthropol. Eurasia* **2015**, *43*, 3–16. [CrossRef]
16. Lbova, L.V.; Kulik, N.A.; Volkov, P.V.; Barkov, A.V.; Vanhaeren, M.; Marchenko, D.V.; Kovalev, V.S. Technology of working with "exotic" mineral resources in the upper palaeolithic of South Siberia (based on the materials of Malaya Syia). *Strat. Plus* **2018**, *1*, 199–211. (In Russian)
17. Shunkov, M.V.; Kulik, N.A.; Kozlikin, M.B.; Sokol, E.V.; Miroshnichenko, L.V.; Ulianov, V.A. The phosphates of Pleistocene-Holocene sediments of the eastern gallery of Denisova Cave. *Dokl. Earth Sci.* **2018**, *478*, 46–50. [CrossRef]
18. Sharygin, V.V.; Wirth, R.; Sokol, E.V.; Nigmatulina, E.N.; Karmanov, N.S. Si-rich natural analog of $Ca_4Ti_2Fe_2O_{11}$ in larnite-gehlenite rock from Hatrurim Basin, Israel. In *3rd International Conference "Crystallogenesis and Mineralogy", Abstract Volume*; Bekker, T.B., Litasov, K.D., Sobolev, N.V., Eds.; Publishing House of SB RAS: Novosibirsk, Russia, 2013; pp. 190–192.
19. Sharygin, V.V.; Yakovlev, G.A.; Wirth, R.; Seryotkin, Y.V.; Sokol, E.V.; Nigmatulina, E.N.; Karmanov, N.S.; Pautov, L.A. Nataliakulikite, IMA 2018-061. CNMNC Newsletter No. 45, October 2018: Page 1230. *Mineral. Mag.* **2018**, *82*, 1225–1232.
20. Becerro, A.I.; McCammon, C.; Langenhorst, F.; Seifert, F.; Angel, R.J. Oxygen-vacancy ordering in $CaTiO_3$–$CaFeO_{2.5}$ perovskites: From isolated defects to infinite sheets. *Phase Transit.* **1999**, *69*, 133–146. [CrossRef]
21. Becerro, A.I.; Carpenter, M.A.; Boffa Ballaran, T.; Seifert, F. Hard mode spectroscopy of $CaTiO_3$–$CaFeO_{2.5}$ perovskites. *Phase Transit.* **2000**, *71*, 161–172. [CrossRef]
22. Becerro, A.I.; Redfern, S.A.T.; Carpenter, M.A.; Knight, K.S.; Seifert, F. Displacive phase transitions in and strain analysis of Fe-dopped $CaTiO_3$ perovskite at high temperatures by neutron diffraction. *J. Solid State Chem.* **2002**, *167*, 459–471. [CrossRef]
23. Mitchell, R.H.; Welch, M.D.; Chakhmouradian, A.R. Nomenclature of the perovskite supergroup: A hierarchical system of classification based on crystal structure and composition. *Mineral. Mag.* **2017**, *81*, 411–461. [CrossRef]
24. Hentschel, G. Mayenit, $12CaO{\cdot}7Al_2O_3$, und Brownmillerit, $2CaO{\cdot}(Al,Fe)_2O_3$, zwei neue Minerale in den Kalksteineinschlüssen der Lava des Ettringer Bellerberges. *N. Jb. Mineral. Mh.* **1964**, 22–29.
25. Chesnokov, B.V.; Bazhenova, L.F. Srebrodolskite $Ca_2Fe_2O_5$—A new mineral. *Zap. Vsesoyuznogo Mineral. Obshchestva* **1985**, *114*, 195–199. (In Russian)
26. Sharygin, V.V.; Sokol, E.V.; Vapnik, Y. Minerals of the pseudobinary perovskite-brownmillerite series from combustion metamorphic larnite rocks of the Hatrurim Formation (Israel). *Russ. Geol. Geophys.* **2008**, *49*, 709–726. [CrossRef]
27. Galuskin, E.V.; Gazeev, V.M.; Armbruster, T.; Zadov, A.E.; Galuskina, I.O.; Pertsev, N.N.; Dzierżanovski, P.; Kadiyski, M.; Gurbanov, A.G.; Wrzalik, R.; et al. Lakargiite $CaZrO_3$: A new mineral of the perovskite group from the Northern Caucasus, Kabardino-Balkaria, Russia. *Am. Mineral.* **2008**, *93*, 1903–1910. [CrossRef]
28. Sharygin, V.V. Minerals of the $Ca_3TiFeAlO_8$–$Ca_3TiFeFeO_8$ series in natural and technogenic pyrometamorphic system. In *The Mineralogy of Technogenesis-2012*; Potapov, S.S., Ed.; Institute of Mineralogy, Uralian Branch of Russian Academy of Sciences: Miass, Russia, 2012; pp. 29–49. (In Russian)
29. Sharygin, V.V.; Wirth, R. Shulamitite and its Fe-analog in metacarbonate xenoliths from alkali basalts, E. Eifel, Germany. In Proceedings of the abstracts of 29th International conference "Ore potential of alkaline, kimberlite and carbonatite magmatism", School "Alkaline magmatism of the Earth", ONTI GEOKHI RAS, Sudak-Moscow, Ukraine-Russia, 14–22 September 2012; pp. 97–99.

30. Sharygin, V.V.; Lazic, B.; Armbruster, T.M.; Murashko, M.N.; Wirth, R.; Galuskina, I.O.; Galuskin, E.V.; Vapnik, Y.; Britvin, S.N.; Logvinova, A.M. Shulamitite $Ca_3TiFe^{3+}AlO_8$—A new perovskite-related mineral from Hatrurim Basin, Israel. *Eur. J. Mineral.* **2013**, *25*, 97–111. [CrossRef]
31. Juroszek, R.; Krüger, H.; Galuskina, I.O.; Krüger, B.; Jeżak, L.; Ternes, B.; Wojdyla, J.; Krzykawski, T.; Pautov, L.A.; Galuskin, E.V. Sharyginite, $Ca_3TiFe_2O_8$, a new mineral from the Bellerberg Volcano, Germany. *Minerals* **2018**, *8*, 308. [CrossRef]
32. Vapnik, Y.; Sokol, E.; Murashko, M.; Sharygin, V. The enigma of Hatrurim. *Mineral. Alm.* **2006**, *10*, 69–77.
33. Gross, S.; Heller, L. A natural occurrence of bayerite. *Mineral. Mag.* **1963**, *33*, 723–724. [CrossRef]
34. Gross, S. Bentorite, a new mineral from the Hatrurim area, West of the Dead Sea, Israel. *Isr. J. Earth Sci.* **1980**, *29*, 81–84.
35. Gross, S. Occurrence of ye'elimite and ellestadite in an unusual cobble from the "pseudo-conglomerate" of the Hatrurim Basin, Israel. *Geol. Surv. Isr. Curr. Res.* **1983**, *84*, 1–4.
36. Weber, D.; Bischoff, A. Grossite ($CaAl_4O_7$)—A rare phase in terrestrial rocks and meteorites. *Eur. J. Mineral.* **1994**, *6*, 591–594. [CrossRef]
37. Murashko, M.N.; Chukanov, N.V.; Mukhanova, A.A.; Vapnik, Y.; Britvin, S.N.; Krivovichev, S.V.; Polekhovsky, Y.S.; Ivakin, I.D. Barioferrite $BaFe^{3+}{}_{12}O_{19}$: A new mineral species of the magnetoplumbite group from the Hatrurim Formation in Israel. *Geol. Ore Depos.* **2011**, *53*, 558–563. [CrossRef]
38. Galuskin, E.V.; Kusz, J.; Armbruster, T.; Galuskina, I.O.; Marzec, K.; Vapnik, Y.; Murashko, M. Vorlanite, $(CaU^{6+})O_4$, from Jabel Harmun, Palestinian Autonomy, Israel. *Am. Mineral.* **2013**, *98*, 1938–1942. [CrossRef]
39. Galuskin, E.V.; Galuskina, I.O.; Kusz, J.; Armbruster, T.; Marzec, K.M.; Dzierżanowski, P.; Murashko, M. Vapnikite Ca_3UO_6—A new double-perovskite mineral from pyrometamorphic larnite rocks of the Jabel Harmun, Palestinian Autonomy, Israel. *Mineral. Mag.* **2014**, *78*, 571–581. [CrossRef]
40. Galuskin, E.V.; Gfeller, F.; Armbruster, T.; Galuskina, I.O.; Vapnik, Y.; Dulski, M.; Murashko, M.; Dzierżanowski, P.; Sharygin, V.V.; Krivovichev, S.V.; et al. Mayenite supergroup, Part III: Fluormayenite, $Ca_{12}Al_{14}O_{32}[\square_4F_2]$ and fluorkyuygenite, $Ca_{12}Al_{14}O_{32}[(H_2O)_4F_2]$, two new minerals from pyrometamorphic rock of the Hatrurim Complex, Southern Levant. *Eur. J. Mineral.* **2015**, *27*, 123–136. [CrossRef]
41. Galuskin, E.V.; Gfeller, F.; Galuskina, I.O.; Pakhomova, A.; Armbruster, T.; Vapnik, Y.; Wlodyka, R.; Dzierżanowski, P.; Murashko, M. New minerals with a modular structure derived from hatrurite from the pyrometamorphic Hatrurim Complex. Part II. Zadovite, $BaCa_6[(SiO_4)(PO_4)](PO_4)_2F$ and aradite, $BaCa_6[(SiO_4)(VO_4)](VO_4)_2F$, from paralavas of the Hatrurim Basin, Negev Desert, Israel. *Mineral. Mag.* **2015**, *79*, 1073–1087. [CrossRef]
42. Galuskin, E.V.; Galuskina, I.O.; Gfeller, F.; Krüger, B.; Kusz, J.; Vapnik, Y.; Dulski, M.; Dzierżanowski, P. Silicocarnotite, $Ca_5[(SiO_4)(PO_4)](PO_4)$, a new "old" mineral from the Negev Desert, Israel, and the ternesite-silicocarnotite solid solution: Indicators of high-temperature alteration of pyrometamorphic rocks of the Hatrurim Complex, Southern Levant. *Eur. J. Mineral.* **2016**, *28*, 105–123. [CrossRef]
43. Galuskin, E.V.; Gfeller, F.; Galuskina, I.O.; Armbruster, T.; Krzatala, A.; Vapnik, Y.; Kusz, J.; Dulski, M.; Gardocki, M.; Gurbanov, A.G.; et al. New minerals with a modular structure derived from hatrurite from the pyrometamorphic rocks. Part III. Gazeevite, $BaCa_6(SiO_4)_2(SO_4)_2O$, from Israel and the Palestine Autonomy, South Levant, and from South Ossetia, Greater Caucasus. *Mineral. Mag.* **2017**, *81*, 499–513. [CrossRef]
44. Galuskina, I.O.; Galuskin, E.V.; Pakhomova, A.S.; Widmer, R.; Armbruster, T.; Krüger, B.; Grew, E.S.; Vapnik, Y.; Dzierżanowski, P.; Murashko, M. Khesinite, $Ca_4Mg_2Fe^{3+}{}_{10}O_4[(Fe^{3+}{}_{10}Si_2)O_{36}]$, a new rhonite-group (sapphirine supergroup) mineral from the Negev Desert, Israel—Natural analogue of the SFCA phase. *Eur. J. Mineral.* **2017**, *29*, 101–116. [CrossRef]
45. Galuskina, I.O.; Galuskin, E.V.; Vapnik, Y.; Prusik, K.; Stasiak, M.; Dzierżanowski, P.; Murashko, M. Gurimite, $Ba_3(VO_4)_2$ and hexacelsian, $BaAl_2Si_2O_8$—Two new minerals from schorlomite-rich paralava of the Hatrurim Complex, Negev Desert, Israel. *Mineral. Mag.* **2017**, *81*, 1009–1019. [CrossRef]
46. Galuskina, I.O.; Krüger, B.; Galuskin, E.V.; Krüger, H.; Vapnik, Y.; Murashko, M.; Agakhanov, A.A.; Pauluhn, A.; Olieric, V. Zoharite, IMA 2017-049. CNMNC Newsletter No. 39, 17, page 1281. *Mineral. Mag.* **2017**, *81*, 1279–1286.
47. Krüger, B.; Krüger, H.; Galuskin, E.V.; Galuskina, I.O.; Vapnik, Y.; Olieric, V.; Pauluhn, A. Aravaite, $Ba_2Ca_{18}(SiO_4)_6(PO_4)_3(CO_3)F_3O$: Modular structure and disorder of a new mineral with single and triple antiperovskite layers. *Acta Crystallogr. Sect. B-Struct. Sci. Cryst. Eng. Mater.* **2018**, *74*, 492–501. [CrossRef]

48. Galuskin, E.V.; Krüger, B.; Galuskina, I.O.; Krüger, H.; Vapnik, Y.; Pauluhn, A.; Olieric, V. Stracherite, $BaCa_6(SiO_4)_2[(PO_4)(CO_3)]F$, the first CO_3-bearing intercalated hexagonal antiperovskite from Negev Desert, Israel. *Am. Mineral.* **2018**, *103*, 1699–1706. [CrossRef]
49. Galuskin, E.V.; Krüger, B.; Galuskina, I.O.; Krüger, H.; Vapnik, Y.; Wojdyla, J.A.; Murashko, M. New mineral with modular structure derived from hatrurite from the pyrometamorphic rocks of the Hatrurim Complex: Ariegilatite, $BaCa_{12}(SiO_4)_4(PO_4)_2F_2O$, from Negev Desert, Israel. *Minerals* **2018**, *8*, 109. [CrossRef]
50. Galuskin, E.V.; Krüger, B.; Galuskina, I.O.; Krüger, H.; Vapnik, Y.; Pauluhn, A.; Olieric, V. Levantite, $KCa_3(Al_2Si_3)O_{11}(PO_4)$, a new latiumite group mineral from pyrometamorphic rock of the Hatrurim Basin, Negev Desert, Israel. *Mineral. Mag.* **2019**, *83*, 1–23. [CrossRef]
51. Galuskina, I.O.; Krüger, B.; Galuskin, E.V.; Krüger, H.; Vapnik, Y.; Banasik, K.; Murashko, M.; Agakhanov, A.A.; Pauluhn, A. Gmalimite, IMA 2019-007. *CNMNC Newsletter No. 50. Mineral. Mag.* **2019**, 83. [CrossRef]
52. Sokol, E.V.; Seryotkin, Y.V.; Kokh, S.N.; Vapnik, Y.; Nigmatulina, E.N.; Goryainov, S.V.; Belogub, E.V.; Sharygin, V.V. Flamite $(Ca,Na,K)_2(Si,P)O_4$, a new mineral from the ultrahigh-temperature combustion metamorphic rocks, Hatrurim Basin, Negev Desert, Israel. *Mineral. Mag.* **2015**, *79*, 583–596. [CrossRef]
53. Britvin, S.N.; Murashko, M.N.; Vapnik, Y.; Polekhovsky, Y.S.; Krivovichev, S.V. Earth's phosphides in Levant and insights into the source of Archean prebiotic phosphorus. *Sci. Rep.* **2015**, *5*, 8355. [CrossRef]
54. Britvin, S.N.; Vapnik, Y.; Polekhovsky, Y.S.; Krivovichev, S.V.; Krzhizhanovskaya, M.G.; Gorelova, L.A.; Vereshchagin, O.S.; Shilovskikh, V.V.; Zaitsev, A.N. Murashkoite, FeP, a new terrestrial phosphide from pyrometamorphic rocks of the Hatrurim Formation, South Levant. *Mineral. Petrol.* **2018**, *113*, 237–248. [CrossRef]
55. Britvin, S.N.; Murashko, M.N.; Vapnik, Y.; Polekhovsky, Y.S.; Krivovichev, S.V.; Vereshchagin, O.S.; Vlasenko, N.S.; Shilovskikh, V.V.; Zaitsev, A.N. Zuktamrurite, FeP_2, a new mineral, the phosphide analogue of löllingite, $FeAs_2$. *Phys. Chem. Miner.* **2019**, *46*, 361–369. [CrossRef]
56. Britvin, S.N.; Murashko, M.N.; Vereshchagin, O.S.; Vapnik, Y.; Shilovskikh, V.V.; Vlasenko, N.S. Polekhovskyite, IMA 2018-147. CNMNC Newsletter No. 48, 19, page 401. *Eur. J. Mineral.* **2019**, *31*, 399–402.
57. Britvin, S.N.; Murashko, M.N.; Krzhizhanovskaya, M.G.; Vereshchagin, O.S.; Vapnik, Y.; Shilovskikh, V.V.; Lozhkin, M.S. Nazarovite, IMA 2019-013. CNMNC Newsletter No. 50. *Mineral. Mag.* **2019**, 83. [CrossRef]
58. Hirsch, F.; Burg, A.; Avni, Y. Geological Map of Israel on a 1:50,000 scale. Arad, Jerusalem, Arad sheet 15–IV. *Geol. Surv. Isr.* **2010**.
59. Vapnik, Y.; Sharygin, V.V.; Sokol, E.V.; Shagam, R. Paralavas in combustion metamorphic complex at the Hatrurim Basin, Israel. *Rev. Eng. Geol.* **2007**, *18*, 133–153. [CrossRef]
60. Sharygin, V.V. A hibonite-spinel-corundum-hematite assemblage in plagioclase-clinopyroxene pyrometamorphic rocks, Hatrurim Basin, Israel: Mineral chemistry, genesis and formation temperatures. *Mineral. Mag.* **2019**, *83*, 123–135. [CrossRef]
61. Kolodny, Y. Natural cement factory: A geological story. In *Cement Production and Use*; Skalny, J., Ed.; Franklin Pierce College: Rindge, NH, USA, 1979; pp. 203–216.
62. Sokol, E.V.; Maksimova, N.V.; Nigmatulina, E.N.; Sharygin, V.V.; Kalugin, V.M. *Combustion Metamorphism*; Izd. SO RAN: Novosibirsk, Russia, 2005. (In Russian)
63. Sokol, E.V.; Novikov, I.S.; Vapnik, Y.; Sharygin, V.V. Gas fire from mud volcanoes as a trigger for the appearance of high-temperature pyrometamorphic rocks of the Hatrurim Formation (Dead Sea area). *Dokl. Earth Sci.* **2007**, *413A*, 474–480. [CrossRef]
64. Sokol, E.V.; Novikov, I.S.; Zateeva, S.N.; Sharygin, V.V.; Vapnik, Y. Pyrometamorphic rocks of the spurrite-merwinite facies as indicators of hydrocarbon discharge zones (the Hatrurim Formation, Israel). *Dokl. Earth Sci.* **2008**, *420*, 608–614. [CrossRef]
65. Bentor, Y.K.; Gross, S.; Heller, L. High temperature minerals in non-metamorphosed sediments in Israel. *Nature* **1963**, *199*, 478–479. [CrossRef]
66. Khoury, H.; Nassir, S. High temperature mineralization in Maqarin area, North Jordan. *N. Jb. Mineral. Abh.* **1982**, *144*, 197–213. [CrossRef]
67. Gur, D.; Steinitz, G.; Kolodny, Y.; Starinsky, A.; McWilliams, M. $^{40}Ar/^{39}Ar$ dating of combustion metamorphism ("Mottled Zone", Israel). *Chem. Geol.* **1995**, *122*, 171–184. [CrossRef]
68. Techer, I.; Khoury, H.N.; Salameh, E.; Rassineux, F.; Claude, C.; Clauer, N.; Pagel, M.; Lancelot, J.; Hamelin, B.; Jacquot, E. Propagation of high-alkaline fluids in an argillaceous formation: Case study of the Khushaym Matruk natural analogue (Central Jordan). *J. Geochem. Explor.* **2006**, *90*, 53–67. [CrossRef]

69. Gilat, A. Hydrothermal activity and hydro-explosions as a cause of natural combustion and pyrolysis of bituminous rocks: The case of Pliocene metamorphism in Israel (Hatrurim Formation). *Geol. Surv. Isr. Curr. Res.* **1998**, *11*, 96–102.
70. Matthews, A.; Gross, S. Petrologic evolution of the "Mottled Zone" (Hatrurim) metamorphic complex of Israel. *Isr. J. Earth Sci.* **1980**, *29*, 93–106.
71. Sharygin, V.V.; Vapnik, Y.; Sokol, E.V.; Kamenetsky, V.S.; Shagam, R. Melt inclusions in minerals of schorlomite-rich veins of the Hatrurim Basin, Israel: Composition and homogenization temperatures. In Proceedings of the ACROFI I: Asian Current Research on Fluid Inclusions, Nanjing University PH, Nanjing, China, 26 May 2006; pp. 189–192.
72. Zateeva, S.N.; Sokol, E.V.; Sharygin, V.V. Specificity of pyrometamorphic minerals of the ellestadite group. *Geol. Ore Depos.* **2007**, *49*, 792–805. [CrossRef]
73. Vapnik, Y.; Galuskina, I.; Palchik, V.; Sokol, E.V.; Galuskin, Y.; Lindsley-Griffin, N.; Stracher, G.B. Stone-tool workshops of the Hatrurim Basin, Israel. In *Coal Peat Fires: A Glob. Perspect. Case Studies-Coal Fires*; Stracher, G.B., Prakash, A., Sokol, E.V., Eds.; Elsevier: Amsterdam, The Netherlands, 2015; Volume 3, pp. 3282–3316. [CrossRef]
74. Pouchou, I.L.; Pichoir, F. "PaP" (phi-rho-z) procedure for improved quantitative microanalysis. In *Microbeam Analysis*; Armstrong, I.T., Ed.; San Francisco Press: San Francisco, CA, USA, 1985; pp. 104–106.
75. Wirth, R. Focused Ion Beam (FIB): A novel technology for advanced application of micro- and nanoanalysis in geosciences and applied mineralogy. *Eur. J. Mineral.* **2004**, *16*, 863–876. [CrossRef]
76. Wirth, R. Focused Ion Beam (FIB) combined with SEM and TEM: Advanced analytical tools for studies of chemical composition, microstructure and crystal structure in geomaterials on a nanometer scale. *Chem. Geol.* **2009**, *261*, 217–229. [CrossRef]
77. Bosi, F.; Hatert, F.; Hålenius, U.; Pasero, M.; Miyawaki, R.; Mills, S.J. On the application of the IMA-CNMNC dominant-valency rule to complex mineral compositions. *Mineral. Mag.* **2019**, *83*, 627–632. [CrossRef]
78. Krause, W.; Nolze, G. POWDER CELL—A program for the representation and manipulation of crystal structures and calculation of the resulting X-ray powder patterns. *J. Appl. Crystallogr.* **1996**, *29*, 301–303. [CrossRef]
79. Prasanna, T.S.R.; Navrotsky, A. Energetics in the brownmillerite-perovskite pseudobinary $Ca_2Fe_2O_5$-$CaTiO_3$. *J. Mater. Res.* **1994**, *9*, 3121–3124. [CrossRef]
80. Žáček, V.; Skála, R.; Chlupáčová, M.; Dvorák, Z. Ca-Fe^{3+}-rich Si-undersaturated buchite from Želénky, North-Bohemian brown coal basin, Czech Republic. *Eur. J. Mineral.* **2005**, *17*, 623–633. [CrossRef]
81. Žáček, V.; Skála, R.; Dvořák, Z. Combustion metamorphism in the Most Basin. In *Coal Peat Fires: A Glob. Perspect. Case Studies-Coal Fires*; Stracher, G.B., Prakash, A., Sokol, E.V., Eds.; Elsevier: Amsterdam, The Netherlands, 2015; Volume 3, pp. 162–202. [CrossRef]
82. Fukuda, K.; Ando, H. Determination of the Pcmn/Ibm2 phase boundary at high temperature in the system $Ca_2Fe_2O_5$–$Ca_2Al_2O_5$. *J. Am. Ceram. Soc.* **2002**, *85*, 1300–1303. [CrossRef]
83. Redhammer, G.J.; Tippelt, G.; Roth, G.; Amthauer, G. Structural variations in the brownmillerite series $Ca_2(Fe_{2-x}Al_x)O_5$: Single-crystal X-ray diffraction at 25 °C and high-temperature powder diffraction (25 °C ≤ T ≤ 1000 °C). *Am. Mineral.* **2004**, *89*, 405–420. [CrossRef]
84. Stöber, S.; Redhammer, G.; Schorr, S.; Prokhnenko, O.; Pöllmann, H. Structure refinements of members in the brownmillerite solid solution series $Ca_2Al_x(Fe_{0.5}Mn_{0.5})_{2-x}O_{5+\delta}$ with 1/2 ≤ x ≤ 4/3. *J. Solid State Chem.* **2013**, *197*, 420–428. [CrossRef]
85. Gloter, A.; Ingrin, J.; Bouchet, D.; Scrivener, K.; Colliex, C. TEM evidence of perovskite-brownmillerite coexistence in the $Ca(Al_xFe_{1-x})O_{2.5}$ system with minor amounts of titanium and silicon. *Phys. Chem. Miner.* **2000**, *27*, 504–513. [CrossRef]
86. Scarlett, N.V.Y.; Pownceby, M.I.; Madsen, I.C.; Christensen, A.N. Reaction sequences in the formation of silico-ferrites of calcium and aluminum in iron ore sinter. *Metall. Mater. Trans. B* **2004**, *35*, 929–936. [CrossRef]
87. Chen, J.; Shevchenko, M.; Hayes, P.C.; Jak, E. A phase equilibrium of the iron-rich corner of the CaO-FeO-Fe_2O_3-SiO_2 system in air and the determination of the SFC primary phase field. *ISIJ Int.* **2019**, *59*, 795–804. [CrossRef]